This is a preprint, the final version is subject to change, of the American Mineralogist (MSA)
Cite as Authors (Year) Title. American Mineralogist, in press.
(DOI will not work until issue is live.) DOI: http://dx.doi.org/10.2138/am-2016-5611

Manuscript 5611 Revision 1

Compositional effects on the solubility of minor and trace elements in oxide spinel minerals: insights from crystal-crystal partition coefficients in chromite exsolution

Vanessa Colás[(a)], José Alberto Padrón-Navarta[(b)], José María González-Jiménez[(c)], William L. Griffin[(d)], Isabel Fanlo[(a)], Suzanne Y. O'Reilly[(d)], Fernando Gervilla[(e)], Joaquín A. Proenza[(f)], Norman J. Pearson[(b)], Monica P. Escayola[(g)]

a. Universidad de Zaragoza, Departamento de Ciencias de la Tierra, Pedro Cerbuna 12, 50009 Zaragoza, Spain.
b. Géosciences Montpellier, CNRS & Univ. Montpellier (UMR5243), 34095, Montpellier, France.
c. Department of Geology and Andean Geothermal Center of Excellence (CEGA), Universidad de Chile, Plaza Ercilla # 803, Santiago, Chile.
d. ARC Centre of Excellence for Core to Crust Fluid Systems (CCFS) and GEMOC National Key Centre, Department of Earth and Planetary Sciences, Macquarie University, Sydney, NSW 2109, Australia.
e. Departamento de Mineralogía y Petrología and Instituto Andaluz de Ciencias de la Tierra (Universidad de Granada-CSIC), Facultad de Ciencias, Avda. Fuentenueva s/n, 18002 Granada, Spain.
f. Departament de Cristal·lografia, Mineralogia i Dipòsits Minerals, Facultat de Geologia, Universitat de Barcelona. Martí i Franquès s/n, 08028 Barcelona, Spain.
g. IDEAN-CONICET, Departamento de Ciencias Geológicas, Facultad de Ciencias Exactas y Naturales, Universidad de Buenos Aires, Intendente Güiraldes 2160, Ciudad Universitaria - Pabellón II -1º EP - Of. 29, (1428) - Buenos Aires, Argentina

To be submitted to American Mineralogist

*Corresponding author: Vanessa Colás
Address: Universidad de Zaragoza, Departamento de Ciencias de la Tierra, Pedro Cerbuna 12, 50009 Zaragoza, Spain.
Phone: +34 976 84 10 98
E-mail: vcolas@unizar.es

This is a preprint, the final version is subject to change, of the American Mineralogist (MSA)
Cite as Authors (Year) Title. American Mineralogist, in press.
(DOI will not work until issue is live.) DOI: http://dx.doi.org/10.2138/am-2016-5611

ABSTRACT

Chromite from Los Congos and Los Guanacos in the Eastern Pampean Ranges of Córdoba (Argentinian Central Andes) shows homogenous and exsolution textures. The composition of the exsolved phases in chromite approaches the end-members of spinel ($MgAl_2O_4$; Spl) and magnetite ($Fe^{2+}Fe^{3+}{}_2O_4$; Mag) that define the corners of the spinel prism at relatively constant Cr^{3+}/R^{3+} ratio (where R^{3+} is $Cr+Al+Fe^{3+}$). The exsolution of these phases from the original chromite is estimated to have accounted at ≥ 600 ºC on the basis of the major-element compositions of chromite with homogenous and exsolution textures that are in equilibrium with forsterite-rich olivine (Fo_{95}). The relatively large size of the exsolved phases in chromite (up to *ca* 200 μm) provided, for the first time, the ability to conduct *in situ* analysis with laser ablation inductively coupled plasma mass spectrometry for a suite of minor- and trace-elements to constrain their crystal-crystal partition coefficient between the spinel-rich and magnetite-rich phases ($D_i^{Spl/Mag}$). Minor- and trace-elements listed in increasing order of compatibility with the spinel-rich phase are Ti, Sc, Ni, V, Ge, Mn, Cu, Sn, Co, Ga and Zn. $D_i^{Spl/Mag}$ values span more than an order of magnitude, from $D_{Ti}^{Spl/Mag} = 0.30 \pm 0.06$ to $D_{Zn}^{Spl/Mag} = 5.48 \pm 0.63$. Our results are in remarkable agreement with data available for exsolutions of spinel-rich and magnetite-rich phases in other chromite from nature, despite their different Cr^{3+}/R^{3+} ratio. The estimated crystal-crystal partitioning coefficients reflect the effect that crystal-chemistry of the exsolved phases from chromite imposes on all investigated elements, excepting Cu and Sc (and only slightly for Mn). The observed preferential partitioning of Ti and Sc into the magnetite-rich phase is consistent with high-temperature chromite/melt experiments and suggests a significant dependence on Fe^{3+} substitution in the spinel structure. A compositional effect of major-elements on

Ga, Co and Zn is observed in the exsolved phases from chromite but not in the experiments; this might be due to crystal-chemistry differences along the $MgFe_{-1}$-$Al_2Fe^{3+}_{-2}$ exchange vector, which is poorly covered experimentally. This inference is supported by the strong covariance of Ga, Co and Zn observed only in chromite from layered intrusions where this exchange vector is important. A systematic increase of Zn and Co coupled with a net decrease in Ga during hydrous metamorphism of chromitite bodies cannot be explained exclusively by compositional changes of major elements in the chromite (which are enriched in the magnetite component). The most likely explanation is that the contents of minor- and trace-elements in chromite from metamorphosed chromitites are controlled by interactions with metamorphic fluids involved in the formation of chlorite.

Keywords: Chromite exsolution, spinel-magnetite, partition coefficient, minor and trace elements, hydrous metamorphism.

INTRODUCTION

A large body of experimental results show that the partitioning of certain minor and trace elements between chromite and melt (± olivine) is sensitive to oxygen fugacity, temperature (Horn et al. 1994; Nielsen et al. 1994; Nielsen and Beard 2000; Canil 1999, 2002; Connolly and Burnett 2003; Righter et al. 2004, 2006; Wijbrans et al. 2015) and a lesser extent to pressure (Canil 1999, 2002; Mallmann and O'Neill 2009). The effect of composition of major- and minor-elements in chromite has also been experimentally investigated, although less systematically (Horn et al. 1994; Nielsen et al. 1994; Nielsen and Beard 2000; Righter et al. 2006; Mallmann and O'Neill 2009; Wijbrans et al. 2015). These findings have been used to estimate the oxygen fugacity of the mantle source (Lee et al. 2003, 2005; Mallmann and O'Neill, 2009), and more

generally the petrogenesis of chromite-bearing rocks (Paktunc and Cabri 1995; Barnes 1998; Barnes and Roeder 2001; Kamenetsky et al. 2001; Mondal et al. 2006; Righter et al. 2006; Li et al. 2008; Pagé and Barnes 2009; Dare et al. 2009; González-Jiménez et al. 2011, 2015; Perinelli et al. 2014; Zhou et al. 2014).

Several works have suggested that subsolidus modifications such as fluid-rock interactions can significantly disturb magmatic signatures in chromite (e.g., Evans and Frost 1975; Burkhard 1993; Barnes 2000; Barnes and Roeder 2001; Mukherjee et al. 2010; Gervilla et al. 2012; Prabhakar and Bhattacharya 2013; Singh and Singh 2013; Gargiulo et al. 2013) including their pattern of minor- and trace-element abundances (Colás et al. 2014; González-Jiménez et al. 2015; Mukherjee et al. 2015). Fluid-rock interactions below 600-650 ºC result in (1) the crystallization of hydrous phases such as chlorite and antigorite, (2) the enrichment of chromium and ferric iron in the chromite and, eventually, (3) a coeval change in apparent oxygen fugacity (e.g., Evans and Frost 1975; Candia and Gaspar 1997; Barnes 2000; Barnes and Roeder 2001; Gervilla et al. 2012). It is therefore challenging to unravel as to that ultimately contributes to the disturbance of magmatic signatures in chromite. This hampers the interpretation of the complex behavior of minor- and trace-elements observed in chromite from metamorphosed chromitites (e.g., Colás et al. 2014; González-Jiménez et al. 2015) or the evaluation of other possible factors such open-system behavior (i.e. element solubility in the fluid phase) that usually predominate during metamorphism of chromite-bearing rocks (e.g., Barnes 2000; Mukherjee et al. 2015).

To date, experimental investigations (at relevant conditions) of hydrous metamorphism in which chromite became modified both texturally and compositionally are lacking. Therefore the evaluation of the compositional factors controlling the solubility of minor- and trace-elements in these settings relies on explorations from

high-temperature experiments, which may suffer additional complications such as bulk element loss (particularly important for Zn; Wijbrans et al. 2015). An alternative approach to investigating the effect of composition, which has not been explored so far, is to use crystal-crystal element partitioning data from exsolved phases in chromite. Exsolution is a process in which chromite solid solution becomes metaestable below critical temperature, and the initial homogeneous chromite separates into at least two different phases that are in equilibrium with each other. Thus, the effect of the major element composition in chromite will be reflected in those minor- and trace-elements with a crystal-crystal partition coefficient from exsolved phases that is significantly different from unity. Pairs of exsolved phases, with contrasting major element compositions, are relatively common and are developed during post-magmatic cooling (Purvis et al. 1972; Muir and Naldrett 1973; Zarkrzewski 1989; Jan et al. 1992; van der Veen and Maaskant 1995; Appel et al. 2002; Garuti et al. 2003; Tamura and Arai 2004, 2005; Krause et al. 2007; Ahmed et al. 2008) and/or high- to medium-grade metamorphism (Loferski and Lipin 1983; Eales et al. 1988; Candia and Gaspar 1997; Abzalov 1998; Proenza et al. 2008). The advantage of this approach is that the temperature (and potentially the oxygen fugacity) of exsolution can be reasonably constrained from the available experimental and thermodynamic data (Turnock and Eugster 1962; Cremer 1969; Muan 1975; Sack and Ghiorso 1991). However, the limitation of this approach for minor- and trace-elements is directly related with the size of the exsolved phases relative to the spatial resolution of modern laser ablation inductively coupled plasma mass spectrometry (LA-ICP-MS).

In this work we report an exceptional case where the size of the exsolved phases in chromite is large enough to be measured *in situ*, with precision, minor- and trace-elements using laser ablation instruments. Thus, we provide the first assessment of the

compositional effect on the solubility of minor- and some trace-elements in natural chromite, specifically along the $MgFe_{-1}$-$Al_2Fe^{3+}_{-2}$ exchange vector (spinel-magnetite join) in the spinel prism. Note that the name "chromite" is used in this work as a general term for Cr-spinel [$(Mg, Fe^{2+})(Cr, Al, Fe^{3+})_2O_4$] from mafic and ultramafic rocks, rather than the *sensu stricto* definition of chromite as the Fe^{2+}-Cr-rich spinel end-member ($Fe^{2+}Cr_2O_4$; Chr).

SAMPLES AND METHODS

The samples analyzed in this study were collected from outcrops of six ophiolitic chromitite bodies from the metamorphosed ultramafic massifs of Los Congos and Los Guanacos in the southern part of the Eastern Pampean Ranges of Córdoba (Argentinian Central Andes; Proenza et al. 2008). These two massifs are separated by 6 km and mainly consist of highly serpentinised metaharzburgite that enclose bodies of metadunites and metalherzolites, and sills of metagabbro. The location and detailed geological description of the studied ultramafic massifs have been given elsewhere (Proenza et al. 2008; Escayola et al. 2004). Escayola et al. (2004) suggested that these metaultramafic rocks where subjected to four metamorphic events, including: (1) low-grade sea-floor metamorphism, overprinted by (2) granulite-facies metamorphism (7.3-9.4 kbar and 760-860 ºC; Rapela et al. 1998; Martino et al. 2010), (3) retrograde amphibolite-facies metamorphism (3.5-7.3 kbar and 590-730 ºC; Rapela et al. 1998; Martino et al. 2010) and (4) a low-temperature hydrothermal event.

The chromitite bodies show massive (>85 vol% chromite), semi-massive (60-85 vol% chromite) and disseminated (<60 vol% chromite) textures (Table 1). Chromite grains are predominantly subhedral and less frequently anhedral with rounded shapes, and have a fracture network of variable density (Fig. 1). Silicate minerals in the

157 chromitites are mainly antigorite, clinochlore and occasionally clinopyroxene (Fig. 1;
158 Table 1). These minerals are also included in chromite grains. The primary olivine is
159 not preserved (Proenza et al. 2008), whereas the fractures that usually cut across
160 chromite grains are filled with serpentinite, chlorite and less frequently carbonates.

161 The careful study of chromite using transmitted and reflected optical microscopy
162 and scanning electron microscope (JEOL SM 6400 SEM belonging to University of
163 Zaragoza, Spain) reveals the presence of three textural varieties of chromite (Fig. 1;
164 Table 1).

165 *Type I* chromite is optically and compositionally homogeneous and occurs in
166 clinopyroxene-bearing massive, semi-massive and disseminated chromitites from Los
167 Congos and Los Guanacos (Fig. 1a-b; Table 1).

168 *Type II* chromite shows an inhomogeneous (exsolved) texture and occurs in
169 clinopyroxene-free massive, semi-massive and disseminated chromitite samples from
170 Los Congos, but the disseminated chromitite sample was selected in this study. It is
171 composed of a low-reflective phase that is complexly intergrown with a high-reflective
172 phase (Fig. 1c-d; Table 1). The high-reflective phase occurs as coarse, sub-rounded,
173 irregular and lobated blebs (from 5-10 to 150 μm) that are distributed randomly
174 throughout the grains, concentrated in the rims or forming linear strings (Fig. 1c). The
175 low-reflective phase itself contains another set of exsolved high-reflective phases
176 forming very fine lamellae (*ca* 1 μm thick), which are arranged in dense networks with
177 an apparent crystallographic control (Fig. 1d).

178 *Type III* chromite is restricted to clinopyroxene-free massive chromitite samples
179 from Los Congos and Los Guanacos, however only chromitite sample from Los
180 Guanacos were studied (Table 1). This chromite shows an irregular coarse mottling or

symplectic texture composed of variable proportions of high-reflective and low-reflective phases (Fig. 1e-f). The exsolved phases in Type III chromites are coarser (up to *ca* 200 μm) than in the Type II ones (below *ca* 40 μm) (Fig. 1c-f).

The contents of major- and minor-elements in the different phases of these three types of chromite were determined quantitatively using both microprobe and LA-ICP-MS at the Geochemical Analysis Unit at CCFS/GEMOC, Macquarie University, Sydney (Australia). Electron-microprobe analyses (EMPA) were obtained by wavelength-dispersive spectrometer (WDS mode) with a Cameca SX-100 under the following working conditions: 20 kV acceleration voltage, 20 nA beam current and 2-3 μm beam size. Peak counting times were 10 s for Cr, Fe, Ti, V, Mn, Zn, and Ni, 20 s for Mg, and 30 s for Al. Standards used were a combination of natural and synthetic minerals and pure metals. Structural formulae of chromite were calculated assuming stoichiometry, following the procedure of Droop (1987).

LA-ICP-MS analyses were carried out using a New Wave UP 266 laser ablation unit coupled to an Agilent 7500cs ICP-MS. The chromite was analyzed for the following masses: ^{45}Sc, ^{47}Ti, ^{51}V, ^{55}Mn, ^{59}Co, ^{60}Ni, ^{65}Cu, ^{66}Zn, ^{71}Ga, ^{72}Ge and ^{118} Sn. The isotopes ^{29}Si and ^{42}Ca were monitored to control the presence of silicate inclusions. The analyses were conducted using a 30-50 μm beam diameter, 5 Hz frequency and 0.152 mJ/pulse power, during 180 s analysis (60 s for the gas blank and 120 s on the chromite). The smallest beam diameters (~30 μm) were used during the measurement of the small blebs in *Type II* chromite. The GLITTER software (Griffin et al. 2008) was used for data reduction. Count signal *vs* time diagrams were checked during single ablation runs to avoid the ablation of mixtures of low-reflective and high-reflective phases in chromite with exsolution textures (Fig. 1S, Supplementary material). The analyses were calibrated against the NIST 610 silicate glass (National Institute

206 Standards and Technology, Gaithersburg, USA) (Norman et al. 1996). Aluminum
207 values obtained by EPMA were used as internal standard. The basaltic glass BCR-2g
208 (Norman et al. 1998; Gao et al. 2002) and the in-house secondary chromite standard
209 LCR-1 (Lace mine, South Africa; Locmelis et al. 2011) were analyzed as unknowns
210 during each analytical run to check the accuracy and precision of the analyses. The
211 results obtained during the analyses of these two standards display very good
212 reproducibility (0.4%-11.4%) (Table 1S, Supplementary material).

213 # RESULTS

214 **Major element composition**

215 The composition of *Type I* chromite in massive chromitites from Los Congos
216 and Los Guanacos follows a distinctive linear trend defined by an increase of Cr#
217 [Cr/(Cr+Al) in atomic ratio] from 0.47 to 0.72 coeval with a decrease of Mg#
218 [Mg/(Mg+Fe^{2+}) in atomic ratio] from 0.68 to 0.52 (Fig. 2a; Table 2). In Los Guanacos
219 the *Type I* chromite from semi-massive and disseminated chromitites show similar
220 trends but are displaced towards lower Mg# (0.48-0.55 in semi-massive chromitites;
221 0.42-0.52 in disseminated chromitites) (Fig. 2a; Table 2). The ratio of Fe^{3+} to other
222 trivalent cations [Fe^{3+}/R^{3+} = Fe^{3+}/(Fe^{3+}+Al+Cr) in atomic ratio] increases from semi-
223 massive (Fe^{3+}/R^{3+} = 0.08-0.10) to disseminated chromitites (Fe^{3+}/R^{3+} = 0.18-0.26) (Fig.
224 2b; Table 2). It is noteworthy that the massive chromitites show Fe^{3+}/R^{3+} ratio (0.13-
225 0.21) intermediate between these two extremes (Fig. 2b; Table 2). All textural types are
226 poor in TiO_2, consistent with the absence of ilmenite exsolution in chromite.

227 The original composition of *Type III* chromite from Los Guanacos, prior to
228 exsolution, was estimated in individual grains based on EPMA analyses (Table 2) and

229 the areal proportion of the exsolved phases in BSE images, using the Image-J software
230 (Rasband 2007) (Table 1). The composition prior to exsolution of *Type II* chromite from
231 Los Congos could not be integrated due to the fine networks of lamellae in the low-
232 reflective domains (cf. Fig. 1d). The estimated original composition of *Type III*
233 chromite has Cr# (0.55-0.60) and Mg# (0.42-0.49) similar to *Type I* chromite from
234 disseminated chromitite (Cr# = 0.55-0.63 and Mg# = 0.42-0.52) (Fig. 2a and 2c; Table
235 2), but it shows the lowest Cr^{3+}/R^{3+} ratio [$Cr^{3+}/(Cr^{3+}+Fe^{3+}+Al)$ in atomic ratio] (≈ 0.34)
236 and the highest Fe^{3+}/R^{3+} ratio (0.40-0.44) amongst all textural groups (Fig. 2b and 2d;
237 Table 2).

238 The low-reflective phase in *Type II* and *Type III* chromite is rich in spinel ss.
239 (Spl; $MgAl_2O_4$), with higher Mg# (0.56-0.63 in *Type II* chromite and 0.64-0.73 in *Type*
240 *III* chromite) but lower Cr# (0.50-0.54 in *Type II* chromite and 0.41-0.43 in *Type III*
241 chromite) than the high-reflective phase (Mg# = 0.21-0.23 and Cr# = 0.85-0.87 in *Type*
242 *II* chromite; Mg# = 0.29-0.33 and Cr# = 0.76-0.79 in *Type III* chromite), which is rich in
243 magnetite (Mag; $Fe^{2+}Fe^{3+}{}_2O_4$) (Fig. 2c; Table 2). This is depicted in the spinel prism
244 (Fig. 2d), which shows that the exsolved phases plot along a compositional field
245 between the spinel (Fe^{3+}/R^{3+} = 0.12-0.21) and magnetite (Fe^{3+}/R^{3+} = 0.55-0.65) corners
246 (i.e. along the $MgFe_{-1}$-$Al_2Fe^{3+}_{-2}$ exchange vector) (Table 2). In contrast to other
247 exsolved phases in chromite from the literature (e.g., Loferski and Lipin 1983, Tamura
248 and Arai 2004, 2005) the Cr^{3+}/R^{3+} ratio in the exsolutions of spinel-rich and magnetite-
249 rich phases from *Type II* and *Type III* chromite is rather constant (from 0.29 to 0.43 and
250 from 0.30 to 0.37, respectively) (Fig. 2d; Table 2).

251 **Crystal-crystal partition coefficients**

252 Minor- and trace-element concentrations for *Type I* and *Type III* chromite from
253 Los Congos and Los Guanacos are shown in Table 2. Analyses of *Type II* chromite
254 from Los Congos were excluded from the following treatment because the beam size of
255 LA-ICP-MS (~30-50 μm) is larger than the size of the exsolved phases (cf. Fig. 1d), and
256 also because internal normalization with the EPMA data is not straightforward. Table 3
257 shows two statistical tests comparing the concentrations of minor and trace elements in
258 the spinel-rich and magnetite-rich phases in *Type III* chromite. The differences in
259 concentration between the two phases are statistically significant for all elements except
260 for Cu and Sn. These tests also reveal that the difference in Mn is less robust than for
261 the rest of the elements. Assuming that the exsolved phases represent an equilibrium
262 assemblage at a given bulk composition, temperature, pressure and fO_2, a set of spinel-
263 rich/magnetite-rich crystal-crystal partition coefficients can be evaluated from the
264 relative change in concentration of the two exsolved phases. Crystal-crystal empirical
265 partition coefficients are calculated based on the LA-ICP-MS data according to the
266 following expression (1):

267 $$D_i^{Spl/Mag} = \frac{C_i^{Spl}}{C_i^{Mag}} \quad (1)$$

268 where the spinel-rich/magnetite-rich partition coefficient ($D_i^{Spl/Mag}$) of an element *i* is
269 defined as the ratio of the concentration of the element (in ppm) in the pair of
270 exsolutions of spinel-rich (C_i^{Spl}) and the magnetite-rich (C_i^{Mag}) phases. Given the
271 restricted range in major-element composition of the exsolved phases (see above) two
272 approaches can be followed to estimate $D_i^{Spl/Mag}$: (1) averaging partition coefficient
273 values for individual pairs (5 pairs of spatially related phases assumed to have been
274 exsolved from the same grain) and (2) computing partition coefficient values based on

the average composition of six spinel-rich and seven magnetite-rich phases (where no assumptions of pairs are made). The two approaches give nearly identical results, however the averaged partition coefficient for individual pairs was used for comparison (Table 3).

Minor elements. Ti, Ni, V, Mn, Co and Zn have been listed in increasing order of compatibility with the spinel-rich phase (Fig. 3; Table 3). Empirical partition coefficients span more than an order of magnitude, from $D_{Ti}^{Spl/Mag}$ = 0.30 ± 0.06 to $D_{Zn}^{Spl/Mag}$ = 5.48 ± 0.63 (Table 3). Minor elements obtained in this work can be readily compared to EPMA analyses of other exsolved phases in chromite from the literature (Fig. 3; see Appendix for sources), where the exchange vector is systematically along the spinel-magnetite corners and with rather constant Cr^{3+}/R^{3+} ratio for each pair (although variable from pair to pair). All elements are in good agreement except for $D_{v}^{Spl/Mag}$, $D_{Co}^{Spl/Mag}$ and $D_{Zn}^{Spl/Mag}$ which are higher in this study compared to the literature data (0.59 ± 0.11 *vs* 0.31 ± 0.14 for V; 1.85 ± 0.23 *vs* 0.92 ± 0.11 for Co and 5.48 ± 0.63 *vs* 3.32 ± 1.98 for Zn, respectively) (Fig. 3). The general agreement is nevertheless remarkable considering that no attempt has been made to subdivide the literature data based on geological setting, temperature or oxygen fugacity conditions and that Cr^{3+}/R^{3+} ratio in the literature data spans the whole possible range along the miscibility gap (Sack and Ghiorso 1992).

Trace elements. Sc, Ge, Cu, Sn and Ga are listed in increasing order of compatibility with the spinel-rich phase (Table 3), spanning also almost an order of magnitude (from $D_{Sc}^{Spl/Mag}$ = 0.33 ± 0.09 to $D_{Ga}^{Spl/Mag}$ = 2.23 ± 0.40; Table 3).

DISCUSSION

Temperature of the exsolution process

The exsolution of spinel-rich and magnetite-rich phases from a precursor chromite from Los Congos and Los Guanacos seems to be independent of the texture of the chromitite body but always it is restricted to clinopyroxene-free assemblages (Table 1). It is interesting to note that the observed exsolutions are in chromitite samples where the main silicate is antigorite rather than clinochlore (Table 1). Clinochlore (but not antigorite) is the expected phyllosilicate produced during hydrous metamorphism of chromite-olivine bearing rocks under amphibolite- to greenschist-facies conditions (e.g., Gervilla et al. 2012). The extensive occurrence of antigorite might indicate an orthopyroxene-bearing chromitite as the original protolith hosting *Type II* and *Type III* chromite prior to hydration (e.g., Bach et al. 2006; Frost and Beard 2007). However, it is clear that the main factor controlling the exsolution was the Cr^{3+}/R^{3+} ratio of the original chromite (Fig. 2 and 4). Only chromite with Cr^{3+}/R^{3+} ratio < 0.35 (and concomitant high Fe^{3+}/R^{3+} > 0.40) show exsolutions of spinel-rich and magnetite-rich phases (Table 2). This feature has been observed in all previously reported studies of exsolution in chromite (Purvis et al. 1972; Muir and Naldrett 1973; Loferski and Lipin 1983; Eales et al. 1988; Zarkrzewski 1989; Jan et al. 1992; van der Veen and Maaskant 1995; Appel et al. 2002; Garuti et al. 2003; Tamura and Arai 2004, 2005; Krause et al. 2007; Ahmed et al. 2008). The position of the miscibility gap defined by the exsolved phases should be indicative of the temperature of exsolution if some constraints can be put on the composition of the ferromagnesian silicate in equilibrium with the chromite prior to its exsolution (Sack and Ghiorso 1991).

The minimum temperature of the exsolution can be constrained using the composition of homogenous *Type I* chromite from disseminated chromitite bodies from Los Guanacos, which has the lowest Cr^{3+}/R^{3+} ratio (0.44-0.48; Table 2; Fig. 4).

Temperature conditions equal to or higher than 600 ºC are required to preserve this chromite as a homogenous phase, which is independent of the forsterite content of the olivine (Sack and Ghiorso 1991). Isothermal (isobaric) Cr-Al-Fe^{3+} sections of the spinel prism at 600 ºC (Sack and Ghiorso 1991) show that the slope of the empirical tielines joining the pair of exsolutions of spinel-rich and magnetite-rich phases match with those calculated by Sack and Ghiorso (1991) when the equilibrium olivine composition is Fo_{80} or Fo_{95} (Fig. 4a and c). The first situation can apply to exsolved phases in chromite with very similar compositions reported from layered intrusions (Purvis et al. 1972; Muir and Naldrett 1973; Loferski and Lipin 1983; Eales et al. 1988; Zarkrzewski 1989; Jan et al. 1992; van der Veen and Maaskant, 1995; Appel et al. 2002; Garuti et al. 2003; Krause et al. 2007; Ahmed et al. 2008) but is at odds with the presumed setting of the ultramafic rocks from the Argentinian Central Andes (Proenza et al. 2008 and references therein). Therefore, we suggest that an olivine of ~Fo_{95} was in equilibrium with the precursor chromite at around 600 ºC in Los Guanacos (Fig. 4c). This interpretation is consistent with the fact that the relic clinopyroxene associated with *Type I* chromite is highly-magnesian (X_{Mg} = 0.954 ± 0.004) and presumably, cogenetic. Tamura and Arai (2004, 2005) reached a similar conclusion from the Iwanai-dake peridotite complex from Hokkaido (Japan), which in this case was supported by the preservation of magmatic olivine with Fo_{92-95}.

The estimated minimum temperature for the exsolution (*ca* 600 ºC) from Los Guanacos (and most likely also from Los Congos) matches with the thermal conditions of amphibolite-granulite facies metamorphism (590-730 ºC) that is inferred to have affected the ultramafic bodies from the southern part of the Eastern Pampean Ranges of Córdoba (Rapela et al. 1998; Escayola et al. 2004; Martino et al. 2010). Under these conditions in the crust, the inferred minimum temperature for Los Guanacos and Los

Congos precludes the coexistence of hydrous phases with chromite during the exsolution process (Gervilla et al. 2012).

Crystal-chemistry constraints on the partition coefficients

The observed crystal-crystal partition coefficients points to the effect that the crystal-chemistry of the spinel-rich ($MgAl_2O_4$) and magnetite-rich phases ($Fe^{2+}Fe^{3+}{}_2O_4$) has on all investigated elements except Cu and Sn (Table 3). The elements most sensitive to crystal-chemistry could be Zn, Ga, Co, Ni, Ti and Sc (Table 3). On the other hand, Mn is only slightly more compatible in the magnetite-rich phase (Table 3).

Oxide spinel minerals comprise a large group of end-members (e.g., Biagioni and Pasero 2014) with the general formula AB_2O_4 (some of them are included in Table 4). The letters A and B represent a range of elements with different valences, and the formulae are conventionally represented as $(A^{2+})[B^{3+}]_2O_4$ (2-3 spinels) and $(A^{4+})[B^{2+}]_2O_4$ (4-2 spinels), where tetrahedrally and octahedrally coordinated sites are represented with parenthesis () and brackets [] respectively. In normal spinels the tetrahedrally coordinated sites are occupied by A whereas the octahedrally coordinated sites are occupied exclusively by B. In inverse spinels the tetrahedrally coordinated sites are occupied by B cations whereas the octahedrally coordinated sites are occupied by A and B cations: $(B^{3+})[A^{2+}B^{3+}]O_4$ for 2-3 spinels and $(B^{2+})[A^{4+}B^{2+}]O_4$ for 4-2 spinels. Cation distribution and degree of ordering in spinel-type structures have been investigated intensely in the past half-century (e.g., see Price et al. 1982 and references therein). Early models were based on crystal field stabilization energies (e.g., McClure 1957; Dunitz and Orgel 1957) but these were later superseded by calculations of electrostatic lattice energy that showed the important role of ionic radii (O'Neill and Navrotsky 1983), pseudopotential orbital radii (Price et al. 1982), or ionic potential

372 (Bosi et al. 2012; Fregola et al. 2012) in influencing cation site preferences in spinel
373 structures. Different cations and their arrangements in octahedrally and tetrahedrally
374 coordinated sites result in changes of the unit-cell parameter, *a*, as well as, in the
375 oxygen fractional coordinate, *u*-parameter (e.g., Lavina et al. 2002; Stevanović et al.
376 2010). The latter parameter describes the deviation of the ideal cubic close packed
377 (CCP) array and the angular distortion of the octahedrally coordinated oxygen
378 polyhedron from the ideal octahedron; and it has been successfully used to predict the
379 normal or inverse nature of 2-3 and 4-2 spinel end-members (e.g., O'Neill and
380 Navrotsky 1983; Stevanović et al. 2010).

381 It can be envisaged that the observed differences in element partitioning between
382 the spinel-rich and the magnetite-rich phases (and therefore their relative solubility) is
383 ultimately related to their contrasting crystal-chemistry (i.e., larger *a* and lower *u* for
384 magnetite relative to spinel, Table 4). Some possible end-members that might be
385 involved in the observed partitioning are shown in Table 4. Contrary to the expectation
386 there is not to clear correlation between *u* and $D_i^{Spl/Mag}$. For the end-member gahnite
387 ($ZnAl_2O_4$) *a* and *u* are effectively similar to spinel (8.0860 vs 8.0832 Å and 0.2636 vs.
388 0.2624, respectively) (Table 4); this similarity probably explains the enrichment of Zn
389 in the spinel-rich phase relative to the magnetite-rich phase ($D_{Zn}^{Spl/Mag}$ = 5.48 ± 0.63;
390 Table 3). Compared to spinel, the Ga end-member $ZnGa_2O_4$ has also similar *u* (0.2617)
391 but contrasting *a* (8.3300 Å) (Table 4) but it is still more compatible with the spinel-rich
392 phase ($D_{Ga}^{Spl/Mag}$ = 2.23 ± 0.40; Table 3), suggesting that *u* rather than *a* controls the
393 partitioning. However, this inference does not apply to Jacobsite ($MnFe_2O_4$) which is
394 slightly more compatible with the magnetite-rich phase ($D_{Mn}^{Spl/Mag}$ = 0.81 ± 0.15; Table
395 3) despite having *u* (0.2615) similar to the Ga end-member (Table 4). The lack of

correlation between u (and/or a) and $D_i^{Spl/Mag}$ is corroborated by the partition of Cu, which probably is controlled by cuprospinel ($CuFe_2O_4$). In this case, although u is similar to magnetite (0.2550 vs. 0.2548, Table 4) Cu is equally partitioned in both phases ($D_{Cu}^{Spl/Mag}$ = 1.11 ± 0.57; Table 3).

Compared to crystal-melt equilibrium where the ionic radii and the elasticity of the crystal lattice are key parameters controlling partitioning (e.g., Blundy and Wood 1994), the factors controlling crystal-crystal partitioning are less well constrained. An attempt to correlate ionic radii with $D_i^{Spl/Mag}$ shows only a very weak dependency (Fig. 5). Divalent cations with radius greater than 0.65 Å are partitioned in the magnetite-rich phase (Fig. 5a). The correlation for trivalent and tetravalent cations is even less clear (Fig. 5b and c). This is in part due to the degree of ordering (normal *vs* inverse) of the spinel. In inverse and partially-inverse spinels the same trivalent cation in 2-3 spinels (or divalent cations in 4-2 spinels) occupies two different sites, resulting in two apparent ionic radii. This even makes the definition of element partitioning based on bulk analyses ambiguous as by definition they do not distinguish between sites. Moreover, the variable valence states of certain elements (such as V, Ti, Mn or Co) further complicates this picture. The complex interplay between crystal-chemistry and the partitioning of minor- and trace-elements suggests a relative dependence on cell parameters and ionic radii of these elements in spinel-type structures. Nevertheless, the ultimate influence of crystal-chemistry on the partitioning is not yet deciphered, due to the lack of detailed studies about the site preference and valence states of minor- and trace-elements in the spinel structures.

Comparison with chromite/melt element partitioning from high temperature experiments

Since early experimental studies (e.g., Horn et al. 1994) it was noticed that the chromite/melt partitioning of certain minor- and trace-elements is a function of the composition of major-elements in chromite. A direct comparison with our calculated $D^{Spl/Mag}$ is not always straightforward as the main exchange vectors experimentally investigated regarding trivalent cations are mostly limited to $Fe^{3+}Cr_{-1}$ (e.g., Horn et al. 1994) and $AlCr_{-1}$, (Wijbrans et al. 2015; these authors also presented data for two compositions along the vector $Fe^{3+}Al_{-1}$). The remarkable agreement of the partitioning data from the exsolved phases in chromite from this study and from the literature (Fig. 3), spanning all possible ranges of Cr^{3+}/R^{3+} ratio of the solvus (from nearly zero to 0.6; Sack and Ghiorso 1991), suggest that the main factor controlling the partitioning in exsolved phases is not due to variations in Cr^{3+} but due to the exchange vector $Fe^{3+}Al_{-1}$.

High temperature (HT) partitioning experiments for Ti and Sc are consistent among several studies and indicate an increase in $D_{Ti}^{Spl/Mag}$ and $D_{Sc}^{Spl/Mag}$ with increasing Fe^{3+} under otherwise constant pressure and temperature conditions but variable oxygen fugacity (Irving 1978; Horn et al. 1994; Nielsen et al. 1994; Nielsen and Beard 2000). This is consistent with the preference of Ti and Sc for the magnetite-rich phase observed in this study (Fig. 3); these elements are amongst the most sensitive to spinel crystal-chemistry ($D_{Ti}^{Spl/Mag}$ = 0.30 ± 0.06 and $D_{Sc}^{Spl/Mag}$ = 0.33 ± 0.09; Table 3). Recent experiments by Wijbrans et al. (2015) further support the preference of Ti and Sc for Fe^{3+}- and Cr-rich (Al-poor) spinels. These authors also observed only a small compositional effect on $D_{Mn}^{Spl/melt}$ in Fe^{3+}-rich spinels, in line with our observations ($D_{Mn}^{Spl/Mag}$ = 0.81 ± 0.15; Table 3) and with the literature data ($D_{Mn}^{Spl/Mag}$ = 0.83 ± 0.42; Fig. 3). Ni is expected to be more compatible in magnetite (through the trevorite component, $NiFe_2O_4$, with inverse nature; Table 4) than in Al-rich spinels, as found in

444 the present study ($D_{Ni}^{Spl/Mag}$ = 0.42 ± 0.09; Table 3) and in other exsolved phases in
445 chromite from the literature ($D_{Ni}^{Spl/Mag}$ = 0.46 ± 0.28; Fig. 3). However, chromite/melt
446 partitioning experiments performed by Righter et al. (2006) and Wijbrans et al. (2015),
447 did not reveal any clear relationship between the partitioning of Ni in chromite and
448 variations in major-element components, except for the amount of Ni itself (Righter et
449 al. 2006). Furthermore, the compositional effect on the partitioning of V cannot be
450 inferred directly from experimental studies because it is strongly linked to the effects of
451 temperature and oxygen fugacity (Horn et al. 1994; Nielsen et al. 1994; Canil 1999;
452 Toplis and Corgne 2002; Lee et al. 2005; Righter et al. 2006; Mallmann and O'Neill
453 2009).

454 Contrary to our observations (Fig. 3; Table 3), the compositional effect on Ga,
455 Co and Zn partitioning in exsolved phases in chromite with contrasting major-element
456 compositions (Horn et al. 1994; Righter et al. 2006; Wijbrans et al. 2015) has not been
457 reported so far. Wijbrans et al. (2015) reported some experimental challenges regarding
458 these elements at high temperatures (> 1300 ºC) and low oxygen fugacity, explaining it
459 due to the volatility of Zn and Ga and alloying of Co with the Pt wire. Another possible
460 explanation is that these elements are only sensitive to $Fe^{3+}Al_{-1}$ variations, which have
461 been poorly experimentally constrained. If so, partitioning data from the exsolved
462 phases in chromite will represent a valuable source of information about the dependency
463 of Ga, Co and Zn partitioning on compositions along the $MgFe_{-1}$-$Al_2Fe^{3+}_{-2}$ exchange
464 vector; this information could be extrapolated with caution to chromite/melt
465 partitioning.

466 In summary it can be concluded that the results of HT experiments and low
467 temperature (LT) exsolutions in chromite are generally in agreement and suggest a
468 significant dependence of Ti and Sc partitioning on Fe^{3+} substitution in chromite. We

speculate that, rather than temperature, the compositional effect on Ga, Co and Zn observed exclusively in the exsolved phases from chromite is due to crystal-chemistry differences along the $MgFe_{-1}$-$Al_2Fe^{3+}_{-2}$ exchange vector (spinel-magnetite vector). The implications of this inference and some observations that might support it will be further explained below.

IMPLICATIONS

The compositional effect that major-elements has on minor- and trace-element partitioning in the exsolved phases in chromite, as deduced from this study, might give some insights into the origin of some compositional trends (or lack of trends) of chromite reported from different magmatic settings and those associated with metamorphism (Fig. 6; see Appendix for data sources).

The linear positive covariation shown by Co and Zn in chromite from magmatic suites is remarkable and suggests a constant relative solubility of Co and Zn (probably as $CoAl_2O_4$ and $ZnAl_2O_4$, gahnite, end-members in a 1:3 molar proportion; Fig. 6a). Moreover these elements are both correlated (particularly for layered intrusions) with the $MgAl_2O_4$ component in the chromite (Fig. 6a). It is also noteworthy the strong positive correlation between Co and Ga in chromite from layered intrusions (probably suggesting a 6:1 molar mix of $CoAl_2O_4$ and $ZnGa_2O_4$) which is not observed in ophiolitic peridotites nor in lavas (Fig. 6b). Compared to other magmatic settings, major-element compositional variations in chromite from layered intrusions correspond mostly to the exchange vectors $MgFe_{-1}$-$Al_2Fe^{3+}_{-2}$, with minor variations of Cr/(Cr+Al) atomic ratio (e.g., Barnes and Roeder 2001). This further supports our previous suggestion that Zn, Co and Ga partitioning is mostly sensitive to variations in $MgFe_{-1}$-$Al_2Fe^{3+}_{-2}$. As a whole these trends probably reflect gradual compositional changes in

493 chromite in equilibrium with melt (and/or olivine) in response to variations in
494 temperature and/or composition.

495 Our observations have also some implications for our understanding of the
496 disturbance of magmatic patterns in minor- and trace-elements during hydration and
497 metamorphism of chromitite bodies. Chromite in apparent textural equilibrium with
498 chlorite shows a distinctive departure from the magmatic trends discussed above (Fig.
499 6c and d). Chromite associated with chlorite, but particularly those enriched in Fe^{3+} (i.e.,
500 Fe^{3+}-rich chromite), have considerably higher Co and Zn contents than magmatic
501 chromite. Moreover the Co:Zn ratio is higher and more scattered in chlorite-bearing
502 assemblages (Fig. 6c). This increase in Co and Zn is associated with a decrease in Ga
503 particularly in Fe^{3+}-rich chromite (Fig. 6d). Whereas the decrease in Ga could be
504 explained by an important change in the chromite composition, the coeval enrichment
505 of Zn and Co is not consistent with the increase in the Fe_3O_4 component in the chromite,
506 which is less variable related to hydrous metamorphism (Barnes 2000; Barnes and
507 Roeder 2001; Mukherjee et al. 2010, 2015; Gervilla et al. 2012; Prabhakar and
508 Bhattacharya 2013; Singh and Singh 2013; Gargiulo et al. 2013). The most likely
509 explanation is that the contents of minor- and trace-elements in chromite affected by
510 hydrous metamorphism are no longer controlled by the compositional changes of major
511 elements in chromite but potentially to the chemistry of metamorphic fluids (e.g., fluids
512 enriched in Zn and Co; Barnes 2000), which produce an incomplete reaction with
513 magmatic chromite (i.e., presence of chromite cores) and the formation of hydrous
514 phases in equilibrium with metamorphosed chromite (see Figure 7 of Gervilla et al.
515 2012). Element partitioning between metamorphosed chromite and hydrous phases has
516 not yet been thoroughly investigated. Interestingly, Colás (2015) reported chlorite from
517 the metamorphosed chromitites of the Eastern Rhodope with relatively high contents of

Ga (up to 30 ppm) and low contents of Zn and Co (below 15 ppm and 18 ppm, respectively). Therefore, the formation of chlorite by interaction with fluids during hydrous metamorphism might explain the enrichment in Co and Zn coupled with strong depletion in Ga in chromite from metamorphosed chromitites of the Eastern Rhodope, as discussed by Colás et al. (2014).

ACKNOWLEDGMENTS

This research was supported by the project CGL2010-15171 and F.P.I. grant BES-2011-045423 of the Ministerio de Econonía y Competitividad (Spain). Support for this study has also been provided by the FONDECYT #11140005 and 'Millenium Nucleus for Metal Tracing Along Subduction NC130065 to José María González-Jiménez. We wish to thank Steve Barnes and an anonymous reviewer for their careful and constructive comments and Ferdinando Bosi for his proficient editorial handling of this manuscript. The analytical data were obtained using instrumentation funded by DEST Systemic Infrastructure Grants, ARC LIEF, NCRIS, industry partners and Macquarie University. This is a contribution XXX from the ARC Centre of Excellence for Core to Crust Fluid Systems (www.ccfs.mq.edu.au) and XXX in the GEMOC Key Centre (www.gemoc.mq.edu.au).

APPENDIX

Data sources for calculated crystal-crystal partition coefficients

The crystal-crystal partition coefficients of exsolved phases in chromite from previously published data sets were calculated using reported EMPA data for minor-elements. Chromite with exsolution textures come from the layered complexes of Carr Boyd Rocks Complex (Western Australia, Purvis et al. 1972), Giant Nickel Mine

(British Columbia, Muir and Naldrett 1973), Red Lodge district (Montana, USA, Loferski and Lipin 1983), Kuså (Sweden, Zakrzewski 1989), Chilas (Pakistan, Jan et al. 1992), Isua Greenstone Belt (Greenland, Appel et al. 2002) and the Eastern Desert (Egypt, Ahmed et al. 2008); from the Uralian-Alaskan-type complexes of Staré Ransko (Czech Republic, van der Veen and Maaskant 1995), Uktus (Rusia, Garuti et al. 2003) and the Central Ural Mountains (Krause et al. 2007); and from the peridotite complex of Iwanai-dake (Japan, Tamura and Arai 2005).

Data source for minor- and trace-elements in chromite

The data sources for minor- and trace-elements in chromite used in this study consist of previously published and new data sets. Chromite samples are classified based on magmatic setting (ophiolitic peridotites, lavas and layered intrusions) and by metamorphic assemblage (chromite and Fe^{3+}-rich chromite in equilibrium with chlorite).

Reported minor- and trace-element compositions of chromite in ophiolitic peridotites come from the Thetford Mine Ophiolite (Canada; Pagé and Barnes 2009), Ouen Island and Dyne (New Caledonia; González-Jiménez et al. 2011; Colás et al. 2014), Mercedita, Tres Amigos and Rupertina (Cuba; Colás et al. 2014; González-Jiménez et al. 2015), and Luobusa (Tibet, Zhou et al. 2014). Chromite samples of lavas are taken from the East Pacific Rise, Bonin Island (Japan), Thetford Mine Ophiolite (Canada) (Pagé and Barnes 2009), and Solomon Island (Yao 1999) and those of layered intrusions from the Bushveld Complex (South Africa) and the Great Dike (Zimbabwe) (Yao 1999). Data for the metamorphosed chromite come from ophiolitic chromitites of Los Congos and Los Guanacos (Argentina), Central and Eastern Rhodope (Bulgaria, González-Jiménez et al. 2015; Colás et al. 2014), Ouen Island (New Caledonia;

González-Jiménez et al. 2011) and Southeastern Turkey (Akmaz et al. 2014); and those from the greenstone belt of Nuggihalli (India, Mukherjee et al. 2015).

Matlab script to plot spinel prism in 3D

The following is a simple Matlab script to plot the spinel prism that reads an input csv file consisting in four columns (without headers) as follow Cr/R^{3+}, Al/R^{3+}, Cr/R^{3+}, and X_{Mg} in mole proportions.

```
clear all
data   = importdata('CongosExs.csv');
lambda = data(:,1:3);
points_x = transpose(1-data(:,4));

% Cartesian components of the triangle vertices r1, r2, r3;
% ri = (yi, zi), i=1:3
%         r1 r2 r3
vertex = [0 1 0.5; % y
          0 0 1];  % z

% transformation to cartesian coordiantes
points_y = zeros(1,length(lambda));
points_z = zeros(1,length(lambda));

for i=1:length(lambda)
    points_y(i) = lambda(i,1)*vertex(1,1)...
        +lambda(i,2)*vertex(1,2)...
+lambda(i,3)*vertex(1,3);
    points_z(i) = lambda(i,1)*vertex(2,1)...
        +lambda(i,2)*vertex(2,2)...
```

```
        +lambda(i,3)*vertex(2,3);
end

scatter3(points_x,points_y,points_z)
xlabel('x'), ylabel('y'), zlabel('z'),
xlim([0 1]), zlim([0 1])
text(-0.05,-0.15,0,['Pc'],'FontSize',14)
text(-0.05,1.15,-0.1,['Sp'],'FontSize',14)
text(1,-0.15,0,['Chr'],'FontSize',14)
text(0,0.5,1.1,['Mf'],'FontSize',14)
text(1,0.5,1.1,['Mt'],'FontSize',14)
text(1.15,1.25,-0.1,['Her'],'FontSize',14)
hold on

daspect([1.7 1 1.1753])

% Prism
plot3([0 0 0 0 1 1 1 1 1 0 0 1],...
[0 1 0.5 0 0 1 0.5 0 0.5 0.5 1 1],...
[0 0 1 0 0 0 1 0 1 1 0 0])
```

REFERENCES

Abzalov, M.Z. (1998) Chrome-spinels in gabbro-Wehrlite intrusions of the Pechenga area, Kola Peninsula, Russia: Emphasis on alteration features. Lithos, 43, 109-134.

617 Ahmed, A.H., Helmy, H.M., Arai, S., and Yoshikawa, M. (2008) Magmatic unmixing
618 in spinel from late Precambrian concentrically-zoned mafic-ultramafic intrusions,
619 Eastern Desert, Egypt. Lithos, 104, 85-98.

620 Akmaz, R.M., Uysal, I., and Saka, S. (2014) Compositional variations of chromite and
621 solid inclusions in ophiolitic chromitites from the southeastern Turkey:
622 Implications for chromitite genesis. Ore Geology Reviews, 58, 208-224.

623 Appel, C., Appel, P., and Rollinson, H. (2002) Complex chromite textures reveal the
624 history of an early Archaean layered ultramafic body in West Greenland.
625 Mineralogical Magazine, 66, 1029-1041.

626 Bach, W., Paulick, H., Garrido, C.J., Ildefonse, B., Meurer, W.P., and Humphris, S.E.
627 (2006) Unraveling the sequence of serpentinization reactions: petrography,
628 mineral chemistry, and petrophysics of serpentinites from MAR 15°N (ODP Leg
629 209, Site 1274). Geophysical Research Letters, 33, L13306.

630 Barnes, S.J. (1998) Chromite in Komatiites, 1. Magmatic controls on crystallization and
631 composition. Journal of Petrology, 39, 1689-1720.

632 Barnes, S.J. (2000) Chromite in komatiites, II. Modification during greenschist to mid-
633 amphibolite facies metamorphism. Journal of Petrology, 41, 387-409.

634 Barnes, S.J., and Roeder, P.L. (2001) The range of spinel compositions in terrestrial
635 mafic and ultramafic rocks. Journal of Petrology, 42, 2279-2302.

636 Biagioni, C. and Pasero, M. (2014) The systematics of the spinel-type minerals: An
637 overview. American Mineralogist, 99, 1254-1264.

638 Blundy, J., and Wood, B. (1994) Prediction of crystal melt partition coefficients from
639 elastic moduli. Nature, 372, 452-454.

640 Bosi, F., Hålenius, U., D'Ippolito, V., and Andreozzi, G.B. (2012) Blue spinel crystals
641 in the $MgAl_2O_4$-$CoAl_2O_4$ series: Part II. Cation ordering over short-range and
642 long-range scales. American Mineralogist, 97, 1834-1840.

643 Burkhard, D.J.M. (1993) Accessory chromium spinels: Their coexistence and alteration
644 in serpentinites. Geochimica et Cosmochimica Acta, 57, 1297-1306.

645 Candia, M.A.F., and Gaspar, J.C. (1997) Chromian spinels in metamorphosed
646 ultramafic rocks from Mangabal I and II complexes, Goiás, Brazil. Mineralogy
647 and Petrology, 60, 27-40.

648 Canil, D. (1999) Vanadium partitioning between orthopyroxene, spinel and silicate melt
649 and the redox states of mantle source regions for primary magmas. Geochimica et
650 Cosmochimica Acta, 63, 557-572.

651 Canil, D. (2002) Vanadium in peridotites, mantle redox and tectonic environments:
652 Archean to present. Earth and Planetary Science Letters, 195, 75-90.

653 Colás, V (2015) Modelos de alteración de cromititas ofiolíticas durante el
654 metamorfismo, 240 p. PhD thesis, Univerisidad de Zaragoza, Spain.

655 Colás, V., Gonzalez-Jimenez, J.M., Griffin, W.L., Fanlo, I., Gervilla, F., O'Reilly, S.Y.,
656 Pearson, N.J., Kerestedjian, T., and Proenza, J.A. (2014) Fingerprints of
657 metamorphism in chromite: New insights from minor and trace elements.
658 Chemical Geology, 389, 137-152.

659 Connolly Jr, H.C., and Burnett, D. (2003) On type B CAI formation: experimental
660 constraints on fO_2 variations in spinel minor element partitioning and
661 reequilibration effects. Geochimica et Cosmochimica Acta, 67, 4429-4434.

662 Cremer, V. (1969) Die Mischkristallbildung im System Chromit-Magnetit-Hercynit
663 zwischen 1000 und 500ºC. Jahrbuch für Mineralogie Abhandlungen, 111, 184-
664 205.

665 Dare, S.A.S., Pearce, J.A., McDonald, I., and Styles, M.T. (2009) Tectonic
666 discrimination of peridotites using fO_2-Cr# and Ga–Ti–Fe^{III} systematics in
667 chrome-spinel. Chemical Geology, 261, 199-216.

668 Droop, G. (1987) A general equation for estimating Fe^{3+} concentrations in
669 ferromagnesian silicates and oxides from microprobe analyses, using
670 stoichiometric criteria. Mineralogical magazine, 51, 431-435.

671 Dunitz, J., and Orgel, L. (1957) Electronic properties of transition-metal oxides-I:
672 Distortions from cubic symmetry. Journal of Physics and Chemistry of Solids, 3,
673 20-29.

674 Eales, H., Wilson, A., and Reynolds, I. (1988) Complex exsolved spinels in layered
675 intrusions within an obducted ophiolite in the Natal-Namaqua mobile belt.
676 Mineralium Deposita, 23, 150-157.

677 Escayola, M., Proenza, J.A., Schalamuk, A., and Cábana, C. (2004) La secuencia
678 ofiolítica de la faja ultramáfica de Sierras Pampeanas de Córdoba, Argentina. In
679 E. Pereira, R. Castroviejo and F. Ortiz, Eds., Complejos ofiolíticos en
680 Iberoamérica: guías de prospección para metales preciosos, 133-155. Proyecto
681 XIII.1-CYTED, Madrid-España

682 Evans, B.W., and Frost, B.R. (1975) Chrome-spinel in progressive metamorphism-a
683 preliminary analysis. Geochimica et Cosmochimica Acta, 39, 959-972.

684 Forster, R., and Hall, E. (1965) A neutron and X-ray diffraction study of ulvöspinel,
685 Fe_2TiO_4. Acta Crystallographica, 18, 857-862.

686 Fregola, R.A., Bosi, F., Skogby, S., and Hålenius, U. (2012) Cation ordering over short-
687 range and long-range scales in the $MgAl_2O_4$-$CuAl_2O_4$ series. American
688 Mineralogist, 97, 1821-1827.

689 Frost, B.R., and Beard, J.S. (2007) On silica activity and serpentinization. Journal of
690 Petrology, 48, 1351-1368.

691 Gao, S., Liu, X., Yuan, H., Hattendorf, B., Günther, D., Chen, L., and Hu, S. (2002)
692 Determination of forty two major and trace elements in USGS and NIST SRM
693 glasses by laser ablation-inductively coupled plasma-mass spectrometry.
694 Geostandards Newsletter, 26, 181-196.

695 Gargiulo, M., Bjerg, E., and Mogessie, A. (2013) Spinel group minerals in
696 metamorphosed ultramafic rocks from Río de Las Tunas belt, Central Andes,
697 Argentina. Geologica Acta, 11, 133-148.

698 Garuti, G., Pushkarev, E.V., Zaccarini, F., Cabella, R., and Anikina, E. (2003) Chromite
699 composition and platinum-group mineral assemblage in the Uktus Uralian-
700 Alaskan-type complex (Central Urals, Russia). Mineralium Deposita, 38, 312-
701 326.

702 Gervilla, F., Padrón-Navarta, J., Kerestedjian, T., Sergeeva, I., González-Jiménez, J.,
703 and Fanlo, I. (2012) Formation of ferrian chromite in podiform chromitites from

the Golyamo Kamenyane serpentinite, Eastern Rhodopes, SE Bulgaria: a two-stage process. Contributions to Mineralogy and Petrology, 164, 643-657.

González-Jiménez, J.M., Augé, T., Gervilla, F., Bailly, L., Proenza, J.A., and Griffin, W.L. (2011) Mineralogy and geochemistry of platinum-rich chromitites from the mantle-crust transition zone at Ouen Island, New Caledonia ophiolite. The Canadian Mineralogist, 49, 1549-1569.

González-Jiménez, J.M., Locmelis, M., Belousova, E., Griffin, W.L., Gervilla, F., Kerestedjian, T.N., O'Reilly, S.Y., Pearson, N.J., and Sergeeva, I. (2015) Genesis and tectonic implications of podiform chromitites in the metamorphosed ultramafic massif of Dobromirtsi (Bulgaria). Gondwana Research, 27, 555-574.

Griffin, W., Powell, W., Pearson, N., and O'Reilly, S. (2008) GLITTER: data reduction software for laser ablation ICP-MS. In P. Sylvester, Ed., Laser Ablation-ICP-MS in the Earth Sciences. Mineralogical Association of Canada Short Course Series, 40, 204-207.

Hill, R.J., Craig, J.R., and Gibbs, G. (1979) Systematics of the spinel structure type. Physics and Chemistry of Minerals, 4, 317-339.

Horn, I., Foley, S.F., Jackson, S.E,. and Jenner, G.A. (1994) Experimentally determined partitioning of high field strength-and selected transition elements between spinel and basaltic melt. Chemical Geology, 117, 193-218.

Irving, A. J. (1978). A review of experimental studies of crystal/liquid trace element partitioning. Geochimica et Cosmochimica Acta, 42, 743-770.

725 Jan, M., Khan, M., and Windley, B. (1992) Exsolution in Al-Cr-Fe^{+3}-rich spinels from
726 the Chilas mafic-ultramafic complex, Pakistan. American Mineralogist, 77, 1074-
727 1074.

728 Kamenetsky, V.S., Crawford, A.J., and Meffre, S. (2001) Factors controlling chemistry
729 of magmatic spinel: an empirical study of associated olivine, Cr-spinel and melt
730 inclusions from primitive rocks. Journal of Petrology, 42, 655-67.

731 Krause, J., Brügmann, G.E., and Pushkarev, E.V. (2007) Accessory and rock forming
732 minerals monitoring the evolution of zoned mafic–ultramafic complexes in the
733 Central Ural Mountains. Lithos, 95, 19-42.

734 Lavina, B., Salviulo, G., and Della Giusta, A. (2002). Cation distribution and structure
735 modelling of spinel solid solutions. Physics and Chemistry of Minerals, 29, 10-18.

736 Lee, C.A., Brandon, A.D., and Norman, M. (2003) Vanadium in peridotites as a proxy
737 for paleo-fO_2 during partial melting: prospects, limitations, and implications.
738 Geochimica et Cosmochimica Acta, 67, 3045-3064.

739 Lee, C.A., Leeman, W.P., Canil, D., and Li, Z.A. (2005) Similar V/Sc systematics in
740 MORB and arc basalts: implications for the oxygen fugacities of their mantle
741 source regions. Journal of Petrology, 46, 2313-2336.

742 Li, C., Ripley, E.M., Tao, Y., and Mathez, E.A. (2008) Cr-spinel/olivine and Cr-
743 spinel/liquid nickel partition coefficients from natural samples. Geochimica et
744 Cosmochimica Acta, 72, 1678-1684.

745 Lindsley, D.H. (1976) The crystal-chemistry and structure of oxide minerals as
746 exemplified by the Fe-Ti oxides. In D. Rumble, Ed., Oxide Minerals, Reviews in
747 Mineralogy, Mineralogical Society of America, 3, L1-L60.

748 Locmelis, M., Pearson, N.J., Barnes, S.J., and Fiorentini, M.L. (2011) Ruthenium in
749 komatiitic chromite. Geochimica et Cosmochimica Acta, 75, 3645-3661.

750 Loferski, P.J., and Lipin, B.R. (1983) Exsolution in metamorphosed chromite from the
751 Red Lodge district, Montana. American Mineralogist, 68, 777-789.

752 Mallmann, G., and O'Neill, H.S.C. (2009) The crystal/melt partitioning of V during
753 mantle melting as a function of oxygen fugacity compared with some other
754 elements (Al, P, Ca, Sc, Ti, Cr, Fe, Ga, Y, Zr and Nb). Journal of Petrology, 50,
755 1765-1794.

756 Martino, R.D., Guereschi, A.B., and Anzil, P.A. (2010) Metamorphic and tectonic
757 evolution at 31° 36′ S across a deep crustal zone from the Sierra Chica of
758 Córdoba, Sierras Pampeanas, Argentina. Journal of South American Earth
759 Sciences, 30, 12-28.

760 McClure, D.S. (1957) The distribution of transition metal cations in spinels. Journal of
761 Physics and Chemistry of Solids, 3, 311-317.

762 Mondal, S.K., Ripley, E.M., Li, C., and Frei, R. (2006) The genesis of Archaean
763 chromitites from the Nuasahi and Sukinda massifs in the Singhbhum Craton,
764 India. Precambrian Research, 148, 45-66.

765 Muan, A. (1975) Phase relations in chromium oxide-containing systems at elevated
766 temperatures. Geochimica et Cosmochimica Acta, 39, 781-802.

767 Muller, O., and Roy, R. (1974) The major ternary structural families. Springer.

768 Muir, J., and Naldrett, A. (1973) A natural occurrence of two-phase chromium-bearing
769 spinels. The Canadian Mineralogist, 11, 930-939.

770 Mukherjee, R., Mondal, S.K., Rosing, M.T., and Frei, R. (2010) Compositional
771 variations in the Mesoarchean chromites of the Nuggihalli schist belt, Western
772 Dharwar Craton (India): potential parental melts and implications for tectonic
773 setting. Contributions to Mineralogy and Petrology, 160, 865-885.

774 Mukherjee, R., Mondal, S.K., González-Jiménez, J.M., Griffin, W.L., Pearson, N.J., and
775 O'Reilly, S.Y. (2015) Trace-element fingerprints of chromite, magnetite and
776 sulfides from the 3.1 Ga ultramafic–mafic rocks of the Nuggihalli greenstone belt,
777 Western Dharwar craton (India). Contributions to Mineralogy and Petrology, 169,
778 1-23.

779 Nielsen, R.L., and Beard, J.S. (2000) Magnetite–melt HFSE partitioning. Chemical
780 Geology, 164, 21-34.

781 Nielsen, R.L., Forsythe, L.M., Gallahan, W.E., and Fisk, M.R. (1994) Major-and trace-
782 element magnetite-melt equilibria. Chemical Geology, 117, 167-191.

783 Norman, M., Pearson, N., Sharma, A., and Griffin, W. (1996) Quantitative analysis of
784 trace elements in geological materials by laser ablation ICPMS: instrumental
785 operating conditions and calibration values of NIST glasses. Geostandards
786 Newsletter, 20, 247-261.

787 Norman, M., Griffin, W., Pearson, N., Garcia, M., and O'reilly, S. (1998) Quantitative
788 analysis of trace element abundances in glasses and minerals: a comparison of

laser ablation inductively coupled plasma mass spectrometry, solution inductively coupled plasma mass spectrometry, proton microprobe and electron microprobe data. Journal of Analytical Atomic Spectrometry, 13, 477-482.

O'Neill, H.S.C., and Navrotsky, A. (1983) Simple spinels; crystallographic parameters, cation radii, lattice energies, and cation distribution. American Mineralogist, 68, 181-194.

Pagé, P., and Barnes, S.J. (2009) Using trace elements in chromites to constrain the origin of podiform chromitites in the Thetford Mines ophiolite, Québec, Canada. Economic Geology, 104, 997-1018.

Paktunc, A., and Cabri, L. (1995) A proton-and electron-microprobe study of gallium, nickel and zinc distribution in chromian spinel. Lithos, 35, 261-282.

Perinelli, C., Bosi, F., Andreozzi, G.B., Conte, A.M., and Armienti, P. (2014) Geothermometric study of Cr-rich spinels of peridotite mantle xenoliths from northern Victoria Land (Antarctica). American Mineralogist, 99, 839-846.

Prabhakar, N., and Bhattacharya, A. (2013) Origin of zoned spinel by coupled dissolution–precipitation and inter-crystalline diffusion: evidence from serpentinized wehrlite, Bangriposi, Eastern India. Contributions to Mineralogy and Petrology, 166, 1047-1066.

Price, G.D., Price, S.L., and Burdett, J.K. (1982) The factors influencing cation site-preferences in spinels a new mendelyevian approach. Physics and Chemistry of Minerals, 8, 69-76.

Proenza, J., Zaccarini, F., Escayola, M., Cábana, C., Schalamuk, A., and Garuti, G. (2008) Composition and textures of chromite and platinum-group minerals in chromitites of the western ophiolitic belt from Pampean Ranges of Córdoba, Argentina. Ore Geology Reviews, 33, 32-48.

Purvis, A., Nesbitt, R., and Hallberg, J. (1972) The geology of part of the Carr Boyd Rocks Complex and its associated nickel mineralization, Western Australia. Economic Geology, 67, 1093-1113.

Rapela, C., Pankhurst, R., Casquet, C., Baldo, E., Saavedra, J., Galindo, C., and Fanning, C. (1998) The Pampean Orogeny of the southern proto-Andes: Cambrian continental collision in the Sierras de Córdoba. Geological Society, London, Special Publications, 142, 181-217.

Rasband, W. (2007) WS 1997–2007 Image J. Bethesda, MD: US National Institutes of Health.

Righter, K., Campbell, A., Humayun, M., and Hervig, R. (2004) Partitioning of Ru, Rh, Pd, Re, Ir, and Au between Cr-bearing spinel, olivine, pyroxene and silicate melts. Geochimica et Cosmochimica Acta, 68, 867-880.

Righter, K., Leeman, W., and Hervig, R. (2006) Partitioning of Ni, Co and V between spinel-structured oxides and silicate melts: Importance of spinel composition. Chemical Geology, 227, 1-25.

Sack, R.O., and Ghiorso, M.S. (1991) Chromian spinels as petrogenetic indicators: Thermodynamics and petrological applications. American Mineralogist, 76, 827-847.

832 Shannon, R.D. (1976) Revised effective ionic radii and systematic studies of
833 interatomic distances in halides and chalcogenides. Acta Crystallographica, 32,
834 751-767.

835 Singh, A.K., and Singh, R.B. (2013) Genetic implications of Zn-and Mn-rich Cr-spinels
836 in serpentinites of the Tidding Suture Zone, eastern Himalaya, NE India.
837 Geological Journal, 48, 22-38.

838 Stevanović, V., d'Avezac, M., and Zunger, A. (2010) Simple point-ion electrostatic
839 model explains the cation distribution in spinel oxides. Physical Review Letters,
840 105, 075501

841 Tamura, A.N., and Arai, S. (2004) Inhomogeneous spinel in chromitite from the Iwanai-
842 dake peridotite complex, Hokkaido, Japan: variations of spinel unmixing texture
843 and chemical composition. Science reports of Kanazawa University, 48, 9-29.

844 Tamura, A., and Arai, S. (2005) Exsolved spinel in chromitite from the Iwanai-dake
845 peridotite complex, Hokkaido, Japan: A reaction between peridotite and highly
846 oxidized magma in the mantle wedge. American Mineralogist, 90, 473-480.

847 Toplis, M.J., and Corgne, A. (2002) An experimental study of element partitioning
848 between magnetite, clinopyroxene and iron-bearing silicate liquids with particular
849 emphasis on vanadium. Contributions to Mineralogy and Petrology, 144, 22-37.

850 Turnock, A., and Eugster, H. (1962) Fe-Al Oxides: Phase Relationships below 1000°C.
851 Journal of Petrology, 3, 533-565.

van der Veen, A., and Maaskant, P. (1995) Chromian spinel mineralogy of the Staré Ransko gabbro-peridotite, Czech Republic, and its implications for sulfide mineralization. Mineralium Deposita, 30, 397-407.

Wechsler, B.A., and Von Dreele, R. (1989) Structure refinements of Mg_2TiO_4, $MgTiO_3$ and $MgTi_2O_5$ by time-of-flight neutron powder diffraction. Acta Crystallographica Section B: Structural Science, 45, 542-549.

Whitney, D.L., and Evans, B.W. (2010) Abbreviations for names of rock-forming minerals. American Mineralogist, 95, 185-187.

Wijbrans, C., Klemme, S., Berndt, J., and Vollmer, C. (2015) Experimental determination of trace element partition coefficients between spinel and silicate melt: the influence of chemical composition and oxygen fugacity. Contributions to Mineralogy and Petrology, 169, 1-33.

Yao, S. (1999) Chemical composition of chromites from ultramafic rocks: application to mineral exploration and petrogenesis, 174 p. PhD thesis, Macquarie University, Sydney, Australia.

Zakrzewski, M.A. (1989) Chromian spinels from Kusa, Bergslagen, Sweden. American Mineralogist, 74, 448-455.

Zhou, M., Robinson, P.T., Su, B., Gao, J., Li, J., Yang, J., and Malpas, J. (2014) Compositions of chromite, associated minerals, and parental magmas of podiform chromite deposits: The role of slab contamination of asthenospheric melts in suprasubduction zone envrionments. Gondwana Research, 26, 262-283.

FIGURE CAPTIONS

874 **Figure 1.** Back Scattered Electron (BSE) images of the different textures of chromite
875 identified in the studied chromitites. *Type I* chromite from Los Congos (**a**) and Los
876 Guanacos (**b**) with relics of clinopyroxene; *Type II* chromite from Los Congos (**c**, **d**)
877 and *Type III* chromite from Los Guanacos (**e**, **f**). Mineral abbreviations after Whitney
878 and Evans (2010), where antigorite is Atg, chromite is Chr, clinopyroxene is Cpx,
879 magnetite is Mag and spinel is Spl.

880 **Figure 2.** Compositional variations of the different textures of chromite from the
881 studied chromitites in terms of Mg# [$Mg/(Mg+Fe^{2+})$ atomic ratio] versus Cr#
882 [Cr/(Cr+Al) atomic ratio] and the spinel prism. Legend provided as inset in the figure
883 and Matlab script to plot spinel prism in 3D is provided in the Appendix.

884 **Figure 3.** Box chart diagrams illustrating the statistical crystal-crystal partition
885 coefficient of certain minor- and trace-elements in exsolved phases within chromite
886 from this study (grey boxes) and from the literature (white boxes). Elements arranged in
887 increasing order of compatibility with the spinel-rich phase. Data sources are listed in
888 the Appendix.

889 **Figure 4.** Isothermal (isobaric) sections determined at 600 and 550 ºC through the
890 spinel prism calculated by Sack and Ghiorso (1991) for fixed Fe-Mg potentials defined
891 by Fo_{80} (**a**, **b**) and Fo_{95} (**c**, **d**). Legend provided as inset in the figure.

892 **Figure 5.** Plot of crystal-crystal partition coefficients *vs* ionic radii (Shannon 1976;
893 O'Neill and Navrotsky 1983) for divalent cations (**a**), trivalent and tetravalent cations in
894 normal (**b**) and inverse spinels (**c**). Legend provided as inset in the figure.

895 **Figure 6.** Compositional variation in terms of Co ($mol \cdot 10^{-4}$) versus Zn ($mol \cdot 10^{-4}$) and
896 Ga ($mol \cdot 10^{-4}$) in chromite from different magmatic settings (**a**, **b**), and affected by

hydrous metamorphism (**c**, **d**). Legend provided as inset in the figure and data sources are listed in the Appendix.

TABLE CAPTIONS

Table 1. Characterization of the chromitite samples from Los Congos and Los Guanacos ultramafic massifs (Argentina) investigated in this study.

Table 2. Average composition of major-, minor- and trace-elements in chromite grains from Los Congos and Los Guanacos ultramafic massifs (Argentina) analyzed by EMPA and LA-ICP-MS.

Table 3. Statistics of minor- and trace-elements of Type III chromite from Los Guanacos ultramafic massif (Argentina).

Table 4. Oxide spinels, ideal composition and selected structural data.

SUPPLEMENTARY MATERIAL

Figure 1S. Counts signal vs time in LA-ICP-MS analysis of low-reflective and high-reflective phases in Type III chromite from Los Guanacos and mixtures of low-reflective and high-reflective phases in Type II chromite from Los Congos. Legend provided as inset in the figure.

Table 1S. Results of repeated analysis of the BCR-2g and LCR-1 standard by laser ablation ICP-MS (New Wave UP 266) and comparison with literature values.

Figure 1

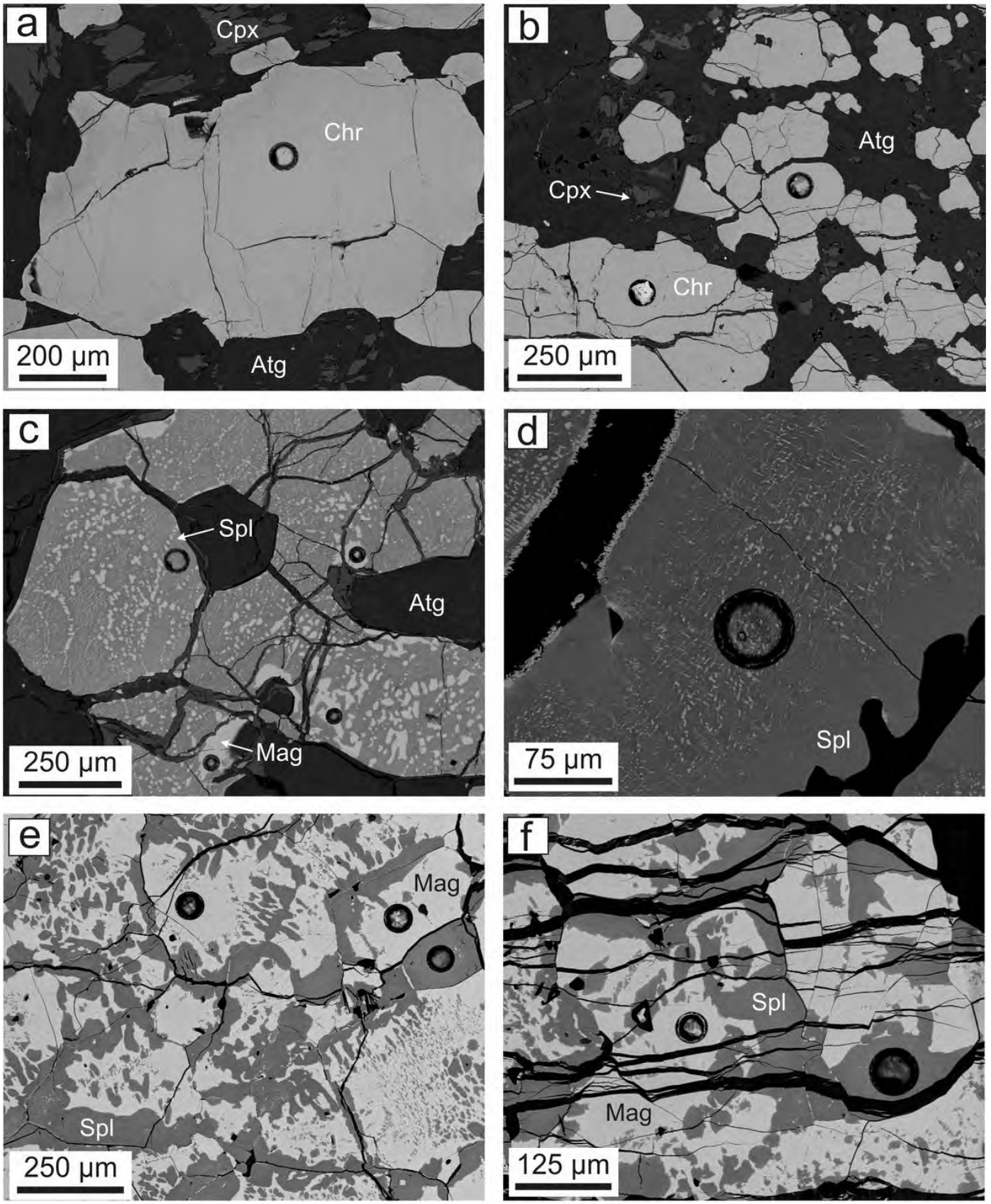
a
Cpx
Chr
Atg
200 µm
b
Atg
Cpx
Chr
250 µm
c
Spl
Atg
Mag
250 µm
d
Spl
75 µm
e
Mag
Spl
250 µm
f
Spl
Mag
125 µm

Figure 2

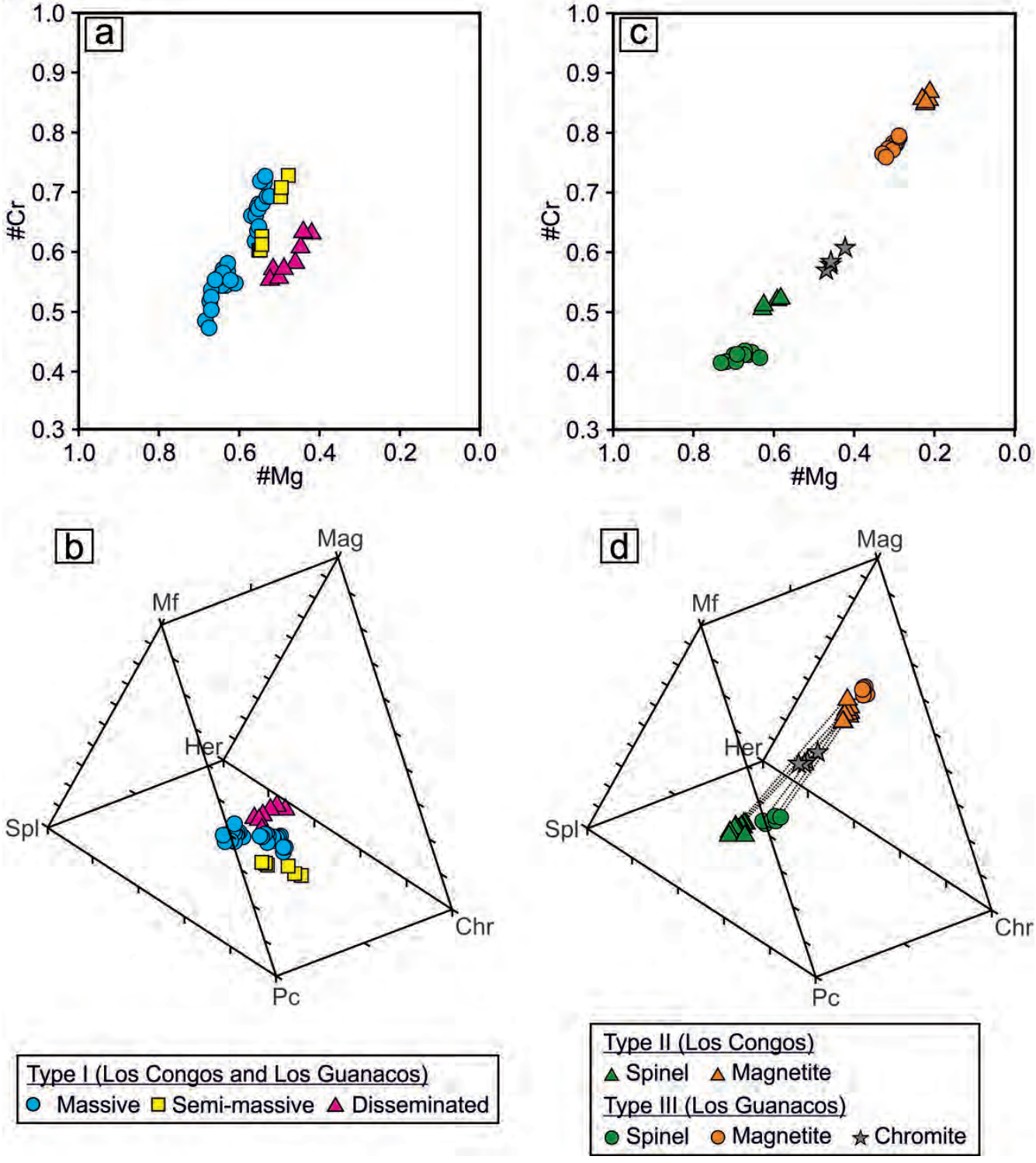
a
1.0
0.9
0.8
0.7
0.6
0.5
0.4
0.3
#Cr
1.0
0.8
0.6
0.4
0.2
0.0
#Mg
c
b
Mag
Mf
Her
Spl
Chr
Pc
d
Type I (Los Congos and Los Guanacos)
Massive
Semi-massive
Disseminated
Type II (Los Congos)
Spinel
Magnetite
Type III (Los Guanacos)
Spinel
Magnetite
Chromite

Figure 3

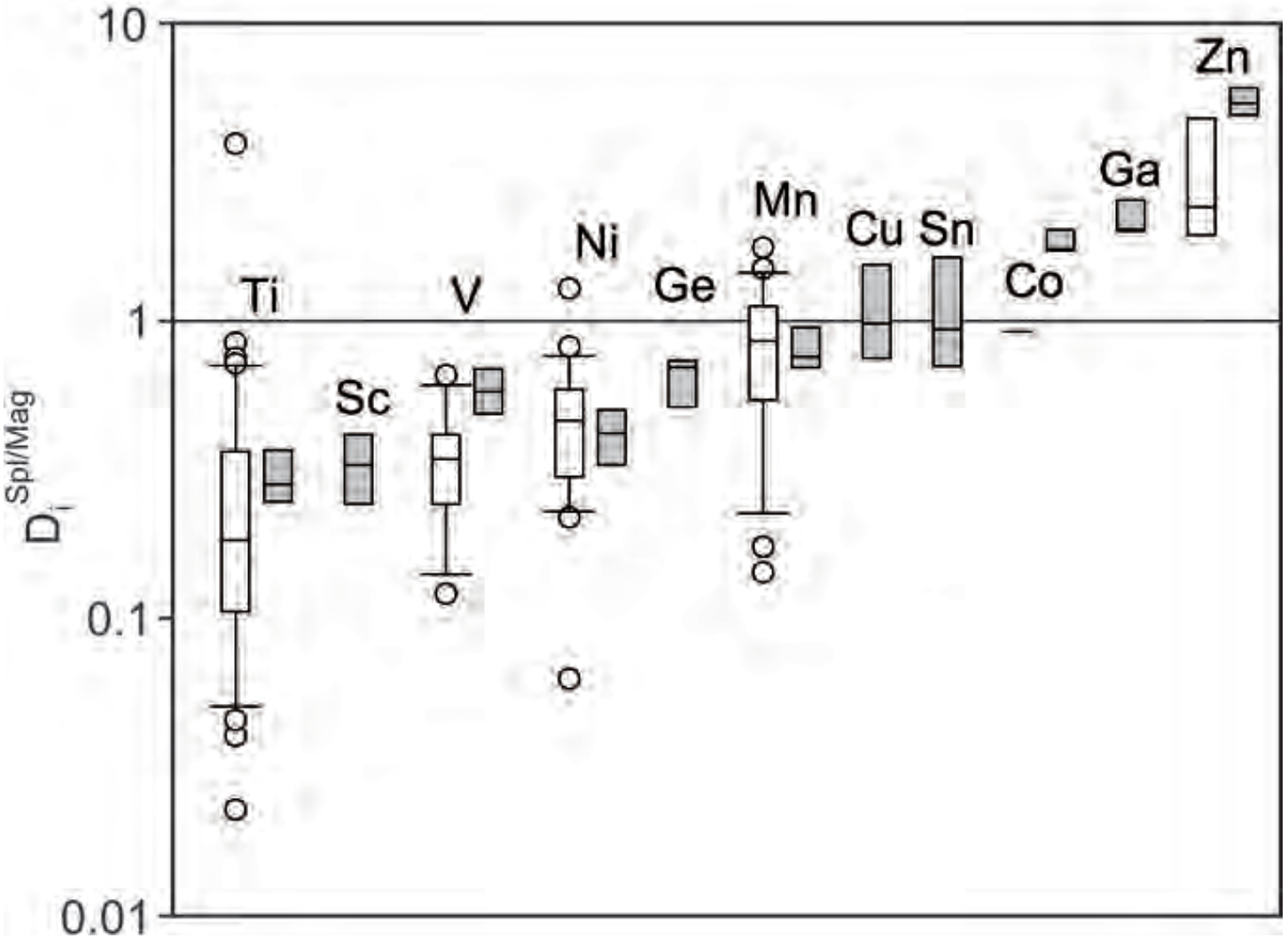

Figure 4

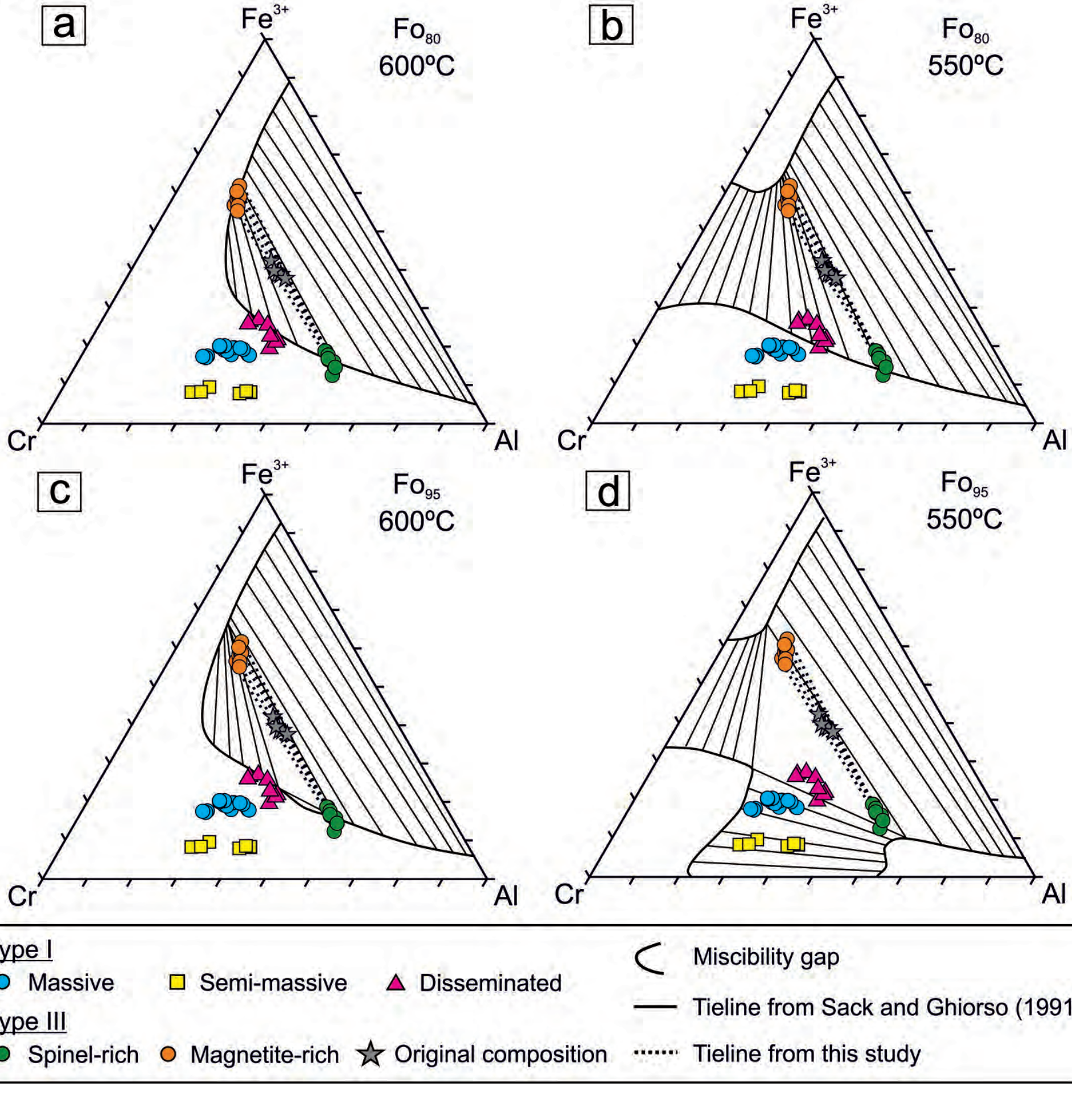
a
Fe3+
Fo80
600ºC
Cr
Al
b
Fe3+
Fo80
550ºC
Cr
Al
c
Fe3+
Fo95
600ºC
Cr
Al
d
Fe3+
Fo95
550ºC
Cr
Al
Type I
Massive
Semi-massive
Disseminated
Type III
Spinel-rich
Magnetite-rich
Original composition
Miscibility gap
Tieline from Sack and Ghiorso (1991)
Tieline from this study

Figure 5

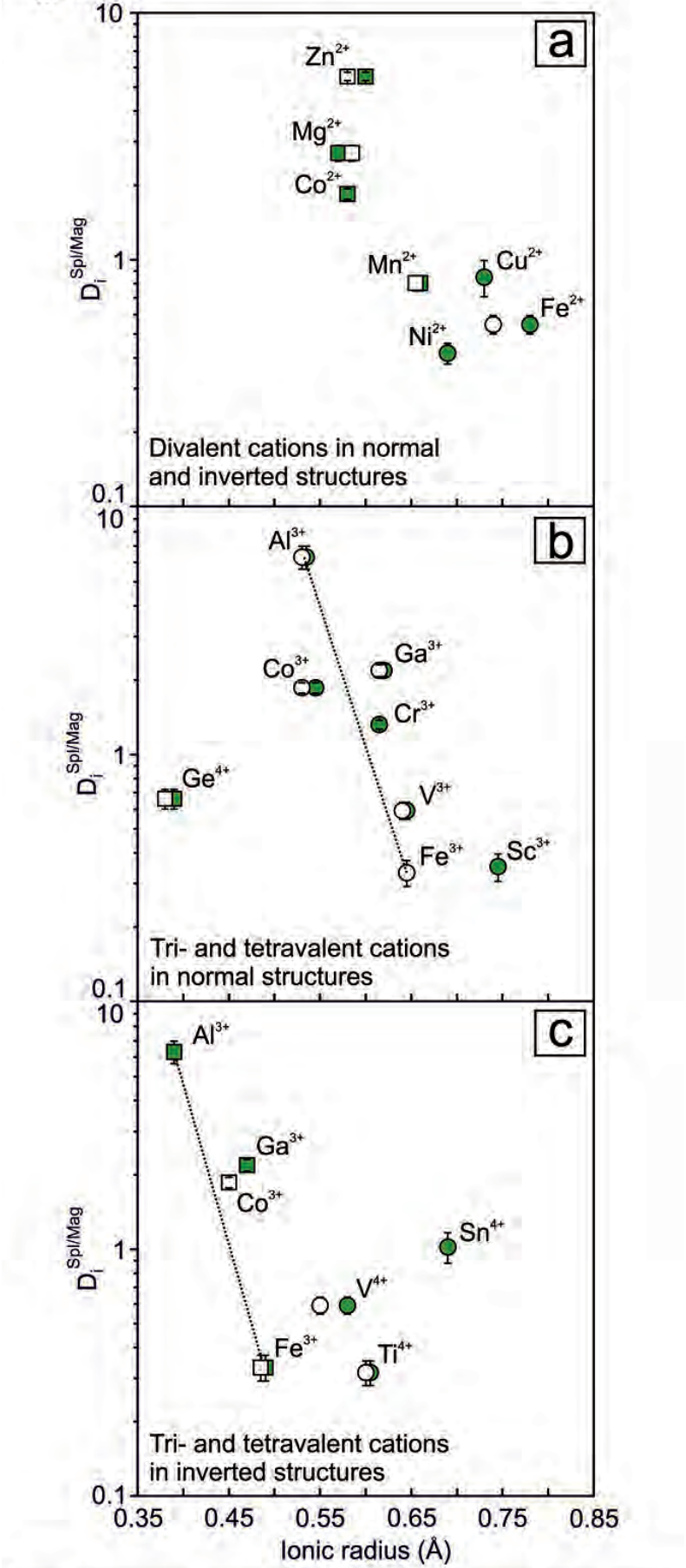

Octahedral coordination
Ionic radius from
- Shannon (1976)
- O´Neill and Navrotsky (1983)

Tetrahedral coordination
Ionic radius from
- Shannon (1976)
- O´Neill and Navrotsky (1983)

Figure 6

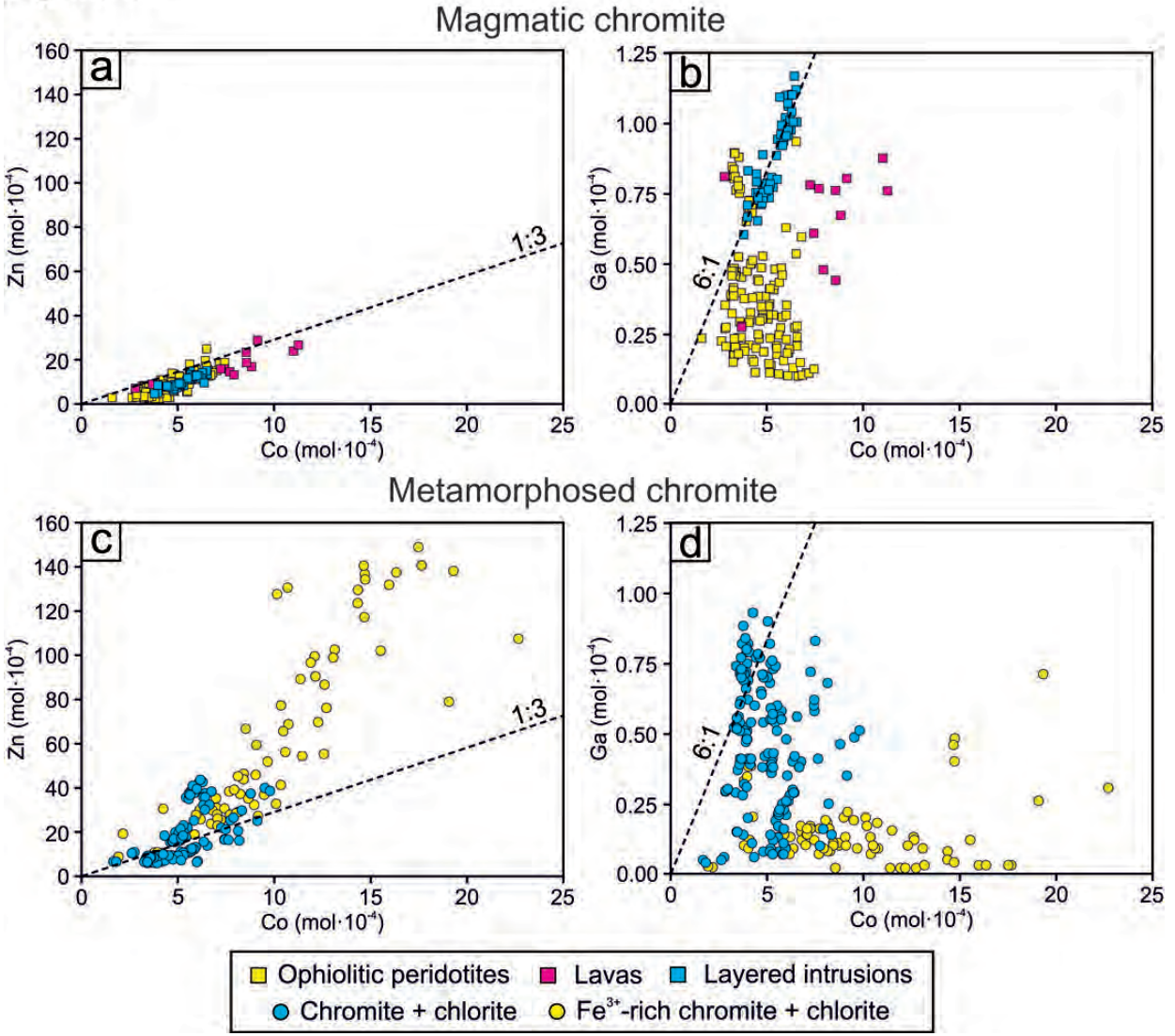
Magmatic chromite
a
b
Zn (mol·10⁻⁴)
Ga (mol·10⁻⁴)
Co (mol·10⁻⁴)
1:3
6:1
Metamorphosed chromite
c
d
Ophiolitic peridotites
Lavas
Layered intrusions
Chromite + chlorite
Fe3+-rich chromite + chlorite

Table 1. Characterization of the chromitite samples from Los Congos and Los Guanacos ultramafic massifs (Argentina) investigated in this study.

Chromite type	Locality	Sample	Chromitite body		Exsolved phase composition	Exsolved phase proportions[a]
			Texture	Silicate matrix		
Type I	Los Congos	M-25	Massive	Atg (10 vol%) Cpx (10 vol%)	Chromite-rich	100%
	Los Guanacos	M-17	Massive	Atg (15 vol%) Cpx (3 vol%) Clc (2 vol%)	Chromite-rich	100%
	Los Guanacos	3317	Semi-massive	Atg (35 vol%) Cpx, (4 vol%) Clc (4 vol%)	Chromite-rich	100%
	Los Guanacos	2260a	Disseminated	Atg (55 vol%) Cpx (7 vol%) Clc (5 vol%)	Chromite-rich	100%
Type II	Los Congos	M-27	Disseminated	Atg (50-70 vol%)	Spinel-rich	na[b]
					Magnetite-rich	na
Type III	Los Guanacos	2226	Massive	Atg (< 20 vol%)	Spinel-rich	39.73%
					Magnetite-rich	60.27%
					Chromite-rich	100%

Note: Mineral abbreviations after Whitney and Evans (2010), where antigorite is Atg, clinochlore is Clc and clinopyroxene is Cpx.

[a] Calculed proportion of each phase in exsolved chromite grains using BSE images on the software Image_J (Rasband 2007). [b] Not available (na)

Table 2. Average composition of major-, minor- and trace-elements in chromite grains from Los Congos and Los Guanacos ultramafic massifs (Argentina) analyzed by EMPA and LA-ICP-MS.

Chromite	Type I				Type II		Type III		
Location	Los Congos		Los Guanacos		Los Congos		Los Guanacos		
Texture	Massive		Semi-massive	Disseminated	Disseminated		Massive		
Sample	M-25	M-17	3317	2260a	M-27		2226		
					Spinel-rich	Magnetite-rich	Spinel-rich	Magnetite-rich	Chromite-rich[a]
	n = 17	n = 16	n = 7	n = 8	n = 6	n = 5	n = 10	n = 9	n = 19
TiO_2 (wt%)[b]	0.19 ± 0.05	0.14 ± 0.02	0.19 ± 0.05	0.19 ± 0.03	0.8 ± 0.83	0.62 ± 0.07	0.05 ± 0.02	0.25 ± 0.01	0.17
Al_2O_3	21.4 ± 2.07	14.16 ± 1.55	17.13 ± 3.04	17.07 ± 2.08	21.02 ± 1.25	2.41 ± 0.11	28.00 ± 1.14	4.50 ± 0.44	13.83
Cr_2O_3	36.79 ± 1.30	42.93 ± 2.00	47.58 ± 2.89	35.92 ± 1.01	33.23 ± 0.74	21.12 ± 0.76	30.63 ± 0.56	23.36 ± 0.87	26.24
Fe_2O_3[c]	14.65 ± 1.85	15.75 ± 0.89	7.03 ± 0.42	18.68 ± 2.08	16.8 ± 0.39	46.28 ± 0.76	14.50 ± 1.69	43.90 ± 1.41	32.22
FeO	13.63 ± 0.75	16.37 ± 0.33	17.99 ± 0.83	19.66 ± 1.12	15.71 ± 1.24	25.27 ± 0.22	12.56 ± 1.06	23.00 ± 0.40	18.86
V_2O_3	0.12 ± 0.02	0.13 ± 0.01	0.19 ± 0.03	0.07 ± 0.02	0.19 ± 0.02	0.36 ± 0.02	0.07 ± 0.03	0.19 ± 0.01	0.14
MnO	0.46 ± 0.03	1.04 ± 0.06	0.40 ± 0.03	0.36 ± 0.05	0.87 ± 0.08	0.9 ± 0.07	0.45 ± 0.03	0.68 ± 0.05	0.59
MgO	14.18 ± 0.59	11.15 ± 0.34	11.01 ± 0.85	9.93 ± 0.95	12.68 ± 0.63	3.97 ± 0.15	15.32 ± 0.81	5.67 ± 0.29	9.50
ZnO	0.09 ± 0.08	0.26 ± 0.03	0.20 ± 0.04	0.12 ± 0.07	0.37 ± 0.07	0 ± 0.00	0.44 ± 0.04	0.09 ± 0.09	0.23
NiO	0.2 ± 0.05	0.22 ± 0.06	0.08 ± 0.07	0.18 ± 0.06	0.19 ± 0.02	0.75 ± 0.02	0.20 ± 0.02	0.75 ± 0.05	0.53
Total	101.8 ± 0.7	102.1 ± 0.4	101.8 ± 0.6	102.3 ± 0.7	101.9 ± 0.79	101.7 ± 0.16	102.2 ± 0.4	102.4 ± 0.4	102.3
Atoms per formula unit calculated on the basis of 4 oxygens									
Al	0.77	0.53	0.64	0.64	0.76	0.10	0.97	0.18	0.53
Cr	0.88	1.08	1.18	0.90	0.81	0.60	0.71	0.64	0.67
Fe^{3+}	0.34	0.38	0.17	0.45	0.39	1.25	0.32	1.15	0.79
V	0.00	0.00	0.00	0.00	0.00	0.01	0.00	0.01	0.00
Mg	0.64	0.53	0.52	0.47	0.58	0.21	0.67	0.29	0.46
Fe^{2+}	0.35	0.44	0.47	0.52	0.40	0.76	0.31	0.67	0.51
Ti	0.00	0.00	0.00	0.00	0.02	0.02	0.00	0.01	0.00
Mn	0.01	0.03	0.01	0.01	0.02	0.03	0.01	0.02	0.02
Ni	0.00	0.01	0.00	0.00	0.00	0.02	0.00	0.02	0.01
Mg#[d]	0.61-0.68	0.52-0.57	0.48-0.55	0.42-0.52	0.56-0.63	0.21-0.23	0.64-0.73	0.29-0.33	0.42-0.49
Cr#[e]	0.47-0.58	0.62-0.72	0.60-0.73	0.55-0.63	0.50-0.54	0.85-0.87	0.41-0.43	0.76-0.79	0.55-0.60
Cr^{3+}/R^{3+}[f]	0.41-0.47	0.51-0.60	0.55-0.67	0.44-0.48	0.40-0.43	0.29-0.32	0.35-0.37	0.30-0.34	0.34
Fe^{3+}/R^{3+}[g]	0.13-0.21	0.17-0.20	0.08-0.10	0.18-0.26	0.19-0.21	0.63-0.65	0.12-0.18	0.55-0.62	0.40-0.44

	n = 11	n = 17	n = 7	n = 6	n = 7	n =13
Sc (ppm)	1.92 ± 0.97	6.00 ± 1.44	0.72 ± 0.38	1.43 ± 0.40	4.10 ± 0.61	3.04
Ti	1159 ± 135	835 ± 96	1011 ± 252	377 ± 94	1198 ± 165	872
V	830 ± 70	775 ± 58	1197 ± 50	668 ± 95	1135 ± 159	950
Mn	3113 ± 157	7457 ± 376	2789 ± 259	3580 ± 372	4455 ± 666	4108
Co	306 ± 10	341 ± 14	381 ± 9	664 ± 33	359 ± 41	480
Ni	1710 ± 337	1609 ± 315	750 ± 80	2133 ± 411	5106 ± 747	3925
Cu	0.82 ± 0.69	2.61 ± 1.87	0.12 ± 0.02	12.11 ± 3.79	14.26 ± 4.09	13.41
Zn	1345 ± 74	2526 ± 164	2261 ± 201	5476 ± 348	991 ± 75	2773
Ga	26.49 ± 2.54	14.77 ± 2.32	24.16 ± 3.49	28.28 ± 1.09	13.01 ± 1.80	19.08
Ge	2.07 ± 0.31	2.48 ± 0.26	1.86 ± 0.27	2.64 ± 0.48	4.01 ± 0.59	3.47
Rb	0.63 ± 0.12	1.77 ± 0.45	0.91 ± 0.28	0.50 ± 0.19	0.44 ± 0.05	0.46
Sn	0.80 ± 0.24	7.14 ± 0.93	1.27 ± 0.21	0.95 ± 0.26	0.94 ± 0.21	0.95

[a] Composition of chromite grains prior to exsolution estimated from the average content and proportions (see Table 1) of spinel-rich and magnetite-rich phases. [b] Uncertainties are given as 1σ standard deviation. [c] Fe_2O_3 contents of chromite were computed assuming R_3O_4 stoichiometry and charge balance. [d] Range of Mg# [Mg/(Mg+Fe^{2+}) atomic ratio]. [e] Range of Cr# [Cr/(Cr+Al) atomic ratio]. [f] Range of Cr^{3+}/R^{3+} ratio [Cr/(Fe^{3+}+Al+Cr) in atomic ratio]. [g] Range of Fe^{3+}/R^{3+} ratio [Fe^{3+}/(Fe^{3+}+Al+Cr) in atomic ratio].

Table 3. Statistics of minor- and trace-elements of Type III chromite from Los Guanacos ultramafic massif (Argentina)[a]

		^{45}Sc	^{47}Ti	^{51}V	^{55}Mn	^{59}Co	^{60}Ni	^{65}Cu	^{66}Zn	^{71}Ga	^{72}Ge	^{118}Sn
$C_i^{Spl\ b}$	Mean	1.43	377	668	3580	664	2133	12.11	5476	28.28	2.64	0.95
(n =6)	Median	1.26	331	620	3444	673	1977	12.49	5456	28.01	2.63	1.05
	Std. Error	0.16	38	39	152	14	168	1.55	142	0.45	0.20	0.11
$C_i^{Mag\ c}$	Mean	4.10	1198	1135	4455	359	5106	14.26	991	13.01	4.01	0.94
(n =7)	Median	4.17	1202	1131	4481	357	5172	15.38	1000	13.34	4.03	0.94
	Std. Error	0.23	63	60	252	16	283	1.54	28	0.68	0.22	0.08
						Comparison of Means						
T test	*p*	2.11E-06	7.45E-07	7.11E-05	1.45E-02	1.65E-08	5.44E-06	3.46E-01	2.74E-07	3.72E-09	7.07E-04	9.22E-01
	Result	R	R	R	R	R	R	**FR**	R	R	R	**FR**
Mann-Witney U	*p*	3.41E-03	3.41E-03	5.34E-03	3.83E-02	3.41E-03	3.41E-03	2.84E-01	3.41E-03	3.41E-03	8.22E-03	9.43E-01
	Result	R	R	R	R	R	R	**FR**	R	R	R	**FR**
						Partition coeficients						
$D_i^{Spl/Mag\ d}$	Mean	0.35	0.31	0.59	0.80	1.85	0.42	0.85	5.52	2.17	0.66	1.01
	Error[e]	0.04	0.04	0.05	0.06	0.09	0.04	0.14	0.21	0.12	0.06	0.14
$D_i^{Spl/Mag\ f}$	Mean	0.33	0.30	0.59	0.81	1.85	0.42	1.11	5.48	2.23	0.64	1.12
	Std. Dev.	0.09	0.06	0.11	0.15	0.23	0.09	0.57	0.63	0.40	0.12	0.70

[a] Reported descriptive statistics are the mean, median, and standard errors of "*n*" samples of each phase from Type III chromite of Los Guanacos. Two statistical tests are also reported comparing the minor and trace elements of spinel-rich with those of magnetite-rich: T test: results of the T test for unequal and unknown variances; Mann-Whitney U test: results of the nonparametric (i.e., no assumptions about the distribution of the underlying population) Mann-Whitney U test. In both tests the null hypothesis is the two means are equal, and the level of significance is 5; p is the empirical significance test of a given test such as $p < 0.05$ indicates a confidence level greater than 0.99; R and FR stand for "reject" and "fail to reject" the null hypothesis, respectively. If rejected, it is likely that the two means are different (i.e., two populations) with a confidence level of p. All statistical computations were carried out using statistical tools from OriginPro (version 15) software. [b, c] Content of the element (in ppm) in the spinel-rich (C_i^{Spl}) and the magnetite-rich (C_i^{Mag}) phases. [d] Average of partition coefficient no assuming pairs. [e] Error of $D_i^{Spl/Mag}$ was calculated using the error propagation furmulae for a division: $\delta D_i^{Spl/Mag} = D_i^{Spl/Mag} \sqrt{(\delta C_i^{Spl}/C_i^{Spl})^2+(\delta C_i^{Mag}/C_i^{Mag})^2}$, where δC_i^{Spl} and δC_i^{Mag} are the standard error of the content of the element (in ppm) in the spinel-rich and magnetite-rich phases, respectively. [f] Average of partition coefficient for individual pairs.

Table 4. Oxide spinels, ideal composition and selected structural data.

Mineral name	Cation A	Cation B	Formulae	x[a]	a (Å)[b]	u[c]
			2-3 spinels ($A^{2+}B^{3+}_2O_4$)			
Hercynite	Fe	Al	$(Fe)[Al]_2O_4$[d]	N(0.00)[h]	8.1490	0.2650
Spinel	Mg	Al	$(Mg)[Al]_2O_4$	N(0.01-0.07)[f,h]	8.0832	0.2624
	Co	Al	$(Co^{2+})[Al]_2O_4$	N(0.15-0.20)[f,h]	8.0950	0.2637
	Cu	Al	$(Cu^{2+})[Al]_2O_4$	N (0.40)[f,h]	8.0860	na[j]
Galaxite	Mn	Al	$(Mn)[Al]_2O_4$	N (0.30)[f,h]	8.2410	0.2650
Gahnite	Zn	Al	$(Zn)[Al]_2O_4$	N(0.00-0.03)[f,h]	8.0860	0.2636
	Fe	Co	$(Co^{3+})[Fe^{2+}Co^{3+}]O_4$	I(1.00)[f,h]	8.2540	na
Chromite	Fe	Cr	$(Fe)[Cr]_2O_4$	N(0.00)[h]	8.3920	na
Magnesiochromite	Mg	Cr	$(Mg)[Cr]_2O_4$	N(0.00)[h]	8.3330	0.2612
	Fe	Ga	$(Fe)[Ga]_2O_4$	I (1.00)[f,h]	8.3600	na
	Zn	Ga	$(Zn)[Ga]_2O_4$	N(0.00)[f,h]	8.3300	0.2617
Magnetite	Fe	Fe	$(Fe^{3+})[Fe^{2+}Fe^{3+}]O_4$	I(1.00)[h]	8.3940	0.2548
Magnesioferrite	Mg	Fe	$(Fe^{3+})[MgFe^{3+}]O_4$	I(0.90)[h]	8.3600	0.2570
	Co	Fe	$(Co^{2+})[Fe]_2O_4$	I(1.00)[f,h]	8.3500	0.2560
Cuprospinel	Cu	Fe	$(Fe^{3+})[CuFe^{3+}]O_4$	I(0.66-1.00)[f,h]	8.3690	0.2550
Jacobsite	Mn	Fe	$(Mn)[Fe^{3+}]_2O_4$	N(0.10-0.15)[f,h]	8.5110	0.2615
Trevorite	Ni	Fe	$(Fe^{3+})[NiFe^{3+}]O_4$	I(1.00)[f,h]	8.3250	0.2573
Coulsonite	Fe	V	$(Fe^{2+})[V^{3+}]_2O_4$	N(0.00)[f,h]	8.4160	0.2598
Magnesiocoulsonite	Mg	V	$(Mg)[V^{3+}]_2O_4$	N(0.00)[f,h]	8.4530	0.2610
			4-2 spinels ($A^{4+}B^{2+}_2O_4$)			
Ulvöspinel	Ti	Fe	$(Fe^{2+})[TiFe^{2+}]O_4$	I(1.00)[e,f,g,h]	8.5300	0.2650
Qandilite	Ti	Mg	$(Mg)[TiMg]O_4$	I(1.00)[f,g,h]	8.4450	0.2650
	V	Fe	$(Fe^{2+})[V^{4+}Fe^{2+}]O_4$	I(1.00)[f,h]	8.4210	na
	V	Mg	$(Mg)[V^{4+}Mg^{2+}]O_4$	I(1.00)[h]	8.3840	0.2610
Brunogeierite	Ge	Fe	$(Ge)[Fe^{2+}]_2O_4$	N(0.00)[f,h]	8.4110	0.2500
	Ge	Mg	$(Ge)[Mg]_2O_4$	N(0.00)[f,h]	8.2496	0.2508
	Sn	Mg	$(Mg)[SnMg]O_4$	I(1.00)[f,h]	8.6000	0.2500

[a]Inversion parameter, where N ($x \leq 0.5$) and I ($x \geq 0.5$) denotes predominantly normal and inverse spinels, respectively. [b]Unit-cell parameter; data from Hill et al. (1979). [c]Oxygen fractional coordinate; data from Hill et al. (1979). [d]The parentheses ( ) and [ ] are used to denote the tetrahedrally and octahedrally coordinated sites, respectively. [e]Forster and Hall (1965). [f]Muller and Roy (1974). [g]Lindsley (1976). [h]Hill et al. (1979). [i]Wechsler and Von Dreele (1989). [j]Not available (na).

Figure 1S

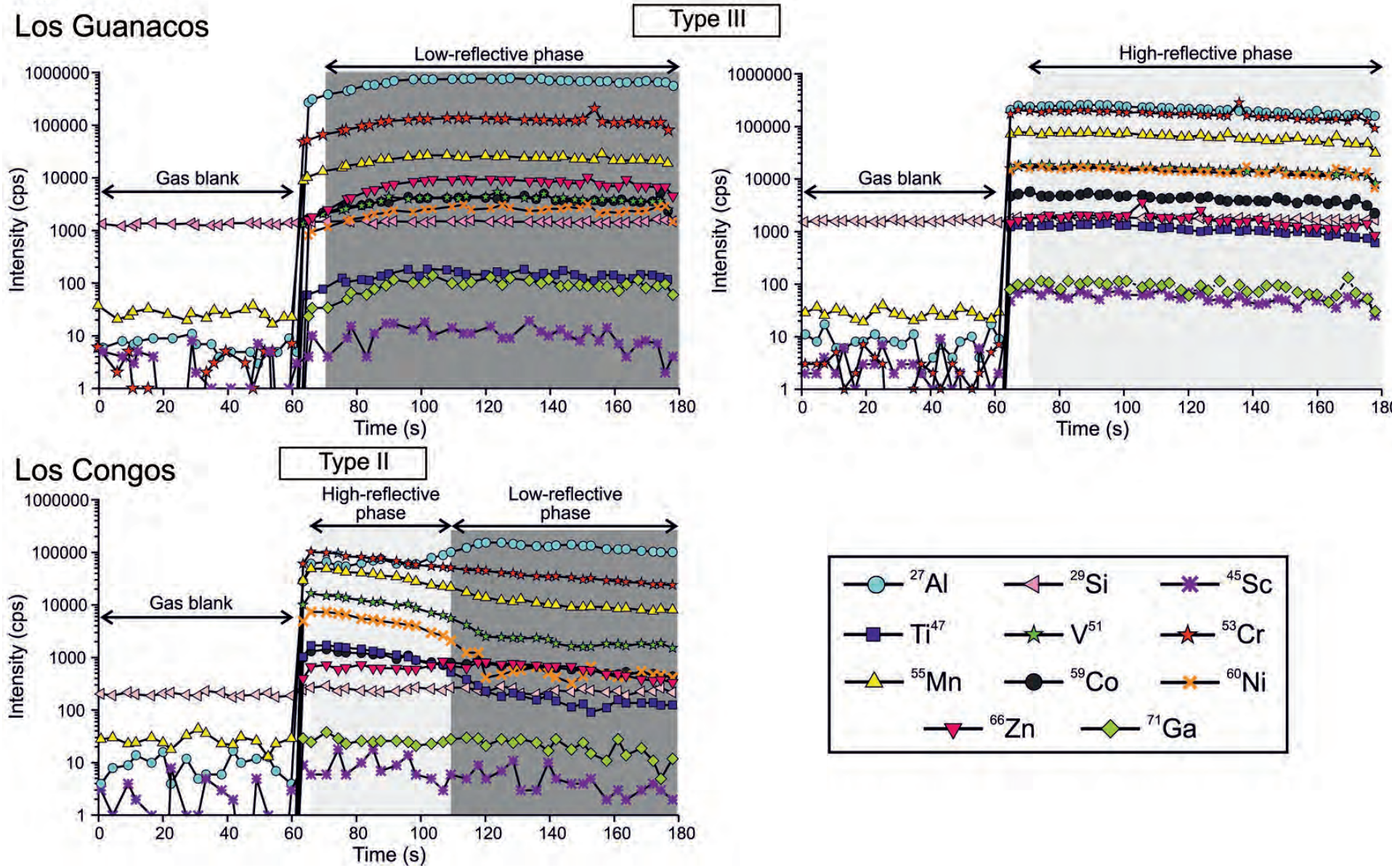
Los Guanacos
Type III
Low-reflective phase
High-reflective phase
Gas blank
Intensity (cps)
Time (s)
Los Congos
Type II
High-reflective phase
Low-reflective phase
Gas blank
Intensity (cps)
Time (s)
27Al
29Si
45Sc
Ti47
V51
53Cr
55Mn
59Co
60Ni
66Zn
71Ga

Table 1S. Results of repeated analysis of the BCR-2g and LCR-1 standard by laser ablation ICP-MS (New Wave UP 266) and comparison with literature values.

	^{45}Sc (ppm)	^{47}Ti	^{51}V	^{55}Mn	^{59}Co	^{60}Ni	^{65}Cu	^{66}Zn	^{71}Ga	^{72}Ge	^{118}Sn
BCR-2g-1	33.82	13794	425	1551	38.34	11.79	18.45	143	22.49	3.06	2.54
BCR-2g-2	32.44	12774	430	1531	39.94	12.50	18.11	151	23.28	2.58	2.41
BCR-2g-3	33.61	12706	435	1567	40.40	13.76	19.14	172	23.78	2.55	2.66
BCR-2g-4	33.25	12823	431	1551	39.34	13.37	18.45	158	23.25	2.95	2.53
BCR-2g-5	33.14	13983	434	1560	38.39	12.08	18.66	149	22.28	2.8	2.51
BCR-2g-6	31.79	12716	431	1551	39.00	12.46	18.94	151	23.52	2.45	2.23
Minimum	31.79	12706	425	1531	38.34	11.79	18.11	143	22.28	2.45	2.23
Maximum	33.82	13983	435	1567	40.40	13.76	19.14	172	23.78	3.06	2.66
Mean	33.01	13133	431	1552	39.24	12.66	18.63	154	23.10	2.73	2.48
Median	33.20	12799	431	1551	39.17	12.48	18.56	151	23.27	2.69	2.52
Std. Dev.	0.8	590	3.3	12.1	0.8	0.8	0.4	10.1	0.6	0.2	0.1
Rel. Dev. (%)	2.3	4.5	0.8	0.8	2.1	6.0	2.0	6.6	2.6	8.9	5.9
Comparison of preferred published value and analyzed value											
Norman et al. (1998)	33	13700	414	na[a]	35.8	10.8	19.4	147	22.7	na	na
Diff. publ. value & this study[b]	-0.01	567	17	na	3.44	1.86	-0.77	7	-0.4	na	na
Dev. publ. value & this study[c]	0.0	4.1	4.1	na	9.6	17.2	-4.0	4.7	-1.8	na	na
Comparison of USGS reference value and analyzed value											
USGS reference value[d]	33	13500	416	1520	37	na	19	127	23	na	na
Diff. USGS value & this study[e]	-0.01	367.18	15	32	-2.24	na	0	27	-0.10	na	na
Dev. USGS value & this study[f]	0.0	2.7	3.6	2.1	-6.0	na	-2.0	21.2	-0.43	na	na

	^{45}Sc (ppm)	^{47}Ti	^{51}V	^{55}Mn	^{59}Co	^{60}Ni	^{65}Cu	^{66}Zn	^{71}Ga	^{72}Ge	^{118}Sn
LCR-1-1	3.47	17323	2333	1825	234	1124	30.22	712	37.97	2.54	2.18
LCR-1-2	3.37	16040	2325	1842	245	1235	29.80	733	39.06	2.48	2.32
LCR-1-3	3.30	15748	2326	1826	247	1227	31.09	754	41.29	2.36	2.28
LCR-1-4	3.35	15764	2335	1827	247	1209	29.90	754	38.70	2.47	2.28
LCR-1-5	3.44	17428	2350	1869	239	1143	30.01	688	39.20	2.83	2.52
LCR-1-6	3.36	16060	2326	1856	252	1249	30.83	776	40.41	3.16	2.17
Minimum	3.30	15748	2325	1825	234	1124	29.80	688	37.97	2.36	2.17
Maximum	3.47	17428	2350	1869	252	1249	31.09	776	41.29	3.16	2.52
Mean	3.38	16394	2332	1841	244	1198	30.31	736	39.44	2.64	2.29
Median	3.37	16050	2329	1835	246	1218	30.12	743	39.13	2.51	2.28
Std. Dev.	0.06	772	9	18	7	52	0.53	32	1.21	0.30	0.13
Rel. Dev. (%)	1.8	4.7	0.4	1.0	2.7	4.3	1.75	4.4	3.1	11.4	5.5
Comparison of preferred published value and analyzed value											
Locmelis et al. (2011)	na	17117	2244	1803	234	1167	na	na	na	na	na
Diff. publ. value & this study[h]	na	723	88	38	9.87	30.70	na	na	na	na	na
Dev. publ. value & this study[i]	na	4.2	3.9	2.1	4.2	2.6	na	na	na	na	na

Note: Al of the NIST610 glass was used as internal standard.

[a] Not analyzed (na). [b] Difference between values published by Norman et al. (1998) and analyzed values. All values were determined by laser ablation ICP-MS. [c] Deviation between values by Norman et al. (1998) and analyzed values. [d] USGS website, September 2015. [e] Difference between USGS reference values and analyzed values. [f] Deviation between USGS reference values and analyzed values. [g] Ratio between USGS reference values and analyzed values. Ratios similar to 0 indicates good reproducibility and ratios near to ±1 indicates non-good reporducibility. [h] Difference between values published by Locmelis et al. (2011) and analyzed values. All values were determined by laser ablation ICP-MS. [i] Deviation between values by Locmelis et al. (2011) and analyzed values.